

Dissecting Local Circuits: Parvalbumin Interneurons Underlie Broad Feedback Control of Olfactory Bulb Output

Kazunari Miyamichi,^{1,3,4} Yael Shlomai-Fuchs,^{2,3} Marvin Shu,¹ Brandon C. Weissbourd,¹ Liqun Luo,^{1,*} and Adi Mizrahi^{2,*}

¹Department of Biology, Howard Hughes Medical Institute, Stanford University, Stanford, CA 94305, USA

²Department of Neurobiology, Institute of Life Sciences, The Edmond and Lily Safra Center for Brain Sciences, The Hebrew University of Jerusalem, Jerusalem 91904, Israel

³These authors contributed equally to this work

⁴Present address: Department of Applied Biological Chemistry and JST ERATO Touhara Chemosensory Signal Project, Graduate School of Agricultural and Life Sciences, The University of Tokyo, Tokyo 113-8657, Japan

*Correspondence: lluo@stanford.edu (L.L.), mizrahi.adi@mail.huji.ac.il (A.M.)

<http://dx.doi.org/10.1016/j.neuron.2013.08.027>

SUMMARY

In the mouse olfactory bulb, information from sensory neurons is extensively processed by local interneurons before being transmitted to the olfactory cortex by mitral and tufted (M/T) cells. The precise function of these local networks remains elusive because of the vast heterogeneity of interneurons, their diverse physiological properties, and their complex synaptic connectivity. Here we identified the parvalbumin interneurons (PVNs) as a prominent component of the M/T presynaptic landscape by using an improved rabies-based transsynaptic tracing method for local circuits. In vivo two-photon-targeted patch recording revealed that PVNs have exceptionally broad olfactory receptive fields and exhibit largely excitatory and persistent odor responses. Transsynaptic tracing indicated that PVNs receive direct input from widely distributed M/T cells. Both the anatomical and functional extent of this M/T → PVN → M/T circuit contrasts with the narrowly confined M/T → granule cell → M/T circuit, suggesting that olfactory information is processed by multiple local circuits operating at distinct spatial scales.

INTRODUCTION

Most brain areas contain highly heterogeneous neural circuits that are spatially intermingled and that serve different functions. Heterogeneity is manifested in diverse cell types, synaptic connectivity patterns, and physiological response profiles (Monyer and Markram, 2004). Understanding information processing by neural circuits, therefore, depends on our ability to identify and study local circuits individually, yet within the context of their larger network. Recent advances in imaging, physiology, and molecular genetics have improved the resolution with which we can identify and functionally isolate neural circuits and their

individual components in the intact brain (Denk et al., 2012; Luo et al., 2008). Here, we combined an improved rabies-based method for transsynaptic tracing of local circuits with in vivo electrophysiology to investigate the unique functional attributes of a particular type of local interneurons in the olfactory bulb (OB) and its synaptic connectivity.

In the OB, olfactory information is represented by two consecutive layers of excitatory neurons, the olfactory receptor neurons (ORNs) and mitral and tufted (M/T) cells. ORNs send afferent axons to the OB where they converge into discrete glomeruli, forming a spatially distributed “odor map” (Sakano, 2010). At the second layer, olfactory information is represented by populations of M/T cells, the output neurons of the OB. Although individual M/T cells receive direct input from a single class of ORNs, olfactory representations in the M/T populations are not a mere reflection of their cognate ORN input (Murthy, 2011). In fact, M/T cells receive a large fraction of their synapses from local interneurons, most of which are inhibitory (Egger and Urban, 2006), and OB local interneurons outnumber M/T cells by two orders of magnitude (Shepherd, 2004).

The local inhibitory networks in the OB are highly diverse in terms of cellular markers (Batista-Brito et al., 2008), morphology (Kosaka and Kosaka, 2011), and physiology (Tan et al., 2010). For example, granule cells (GCs) form a local inhibitory circuit with mitral cells (MCs) via dendrodendritic interactions (Jahr and Nicoll, 1980; Shepherd, 2004). GCs mediate recurrent inhibition whereby GCs inhibit, in a reciprocal manner, the exact same MC that excited them. Additionally, GCs can mediate lateral inhibition between different MCs through inhibition of nearby MCs (Margrie et al., 2001; Shepherd et al., 2007). Other inhibitory networks involving periglomerular neurons have been suggested to contribute to the decorrelation of M/T ensembles, a process suggested to be central for odor discrimination (Aungst et al., 2003; Cleland, 2010). However, the mechanisms by which these and other local networks in the OB transform olfactory information remain poorly understood, partly due to the heterogeneity of the physiological properties and connectivity patterns of interneurons. For example, it remains unclear which local interneuron types provide direct input to M/T cells, and what are their spatial distributions with respect to that of M/T cells.

The rabies virus (RV)-mediated monosynaptic tracing strategy (Wickersham et al., 2007) has been combined with mouse genetics to identify presynaptic partners of defined neuronal subtypes in different regions of the brain and spinal cord. This system utilized a mutant RV, which lacks the rabies gene encoding the envelope glycoprotein (RG) required for viral spread. This mutant RV is pseudotyped with the avian EnvA envelope glycoprotein, which restricts the cells the virus can initially transduce to those that express the EnvA receptor TVA. To reconstitute infectious RV particles in vivo in a defined neuronal population of interest (the “starter cell” population), neurons are first transduced with conditional adeno-associated virus (AAV) vectors that express TVA and RG in a manner that is dependent on the expression of the Cre recombinase (Wall et al., 2010; Watabe-Uchida et al., 2012) or the tetracycline transactivator tTA2 (Miyamichi et al., 2011). The starter cells can thus be restricted to particular populations based on cell-type-specific Cre or tTA2 expression. Neurons expressing TVA and RG can then be transduced by EnvA-pseudotyped and RG-deleted RV to produce starter cells, from which their presynaptic partners are infected by reconstituted RV. Here, we improved upon previous tracing methods so as to more precisely trace connectivity within local circuits. We combined our improved transsynaptic tracing with mouse genetics and in vivo physiology to investigate local interneuron circuits in the mouse OB. Our study suggests that reciprocal connections between M/T cells and parvalbumin neurons (PVNs) underlie a broad feedback control of the OB output.

RESULTS

Optimizing Local Circuit Analysis Using Transsynaptic Tracing

Two technical limitations need to be overcome in order for RV-mediated transsynaptic labeling to be applied for the analysis of local circuit connectivity with precision. First, to achieve unambiguous interpretation of local connections, starter cells should be unequivocally labeled to distinguish them from their presynaptic partners. Second, nonspecific labeling by RV needs to be close to zero to avoid false positives in the identification of presynaptic partners. Currently applied methods suffer from one or both of these limitations (see below). Therefore, we first attempted to optimize the RV method for tracing local circuits.

In the system developed by Watabe-Uchida et al. (2012), starter cells are cotransduced by two AAV vectors that express (1) a TVA-mCherry fusion protein in a Cre-dependent manner and (2) RG to complement RV- Δ G-GFP, allowing transsynaptic tracing from Cre-expressing cells. We found that, depending on the brain region and cell type, starter cells were not consistently detected due to variable expression of mCherry. To improve starter cell identification, we changed the promoter and sequences surrounding the start codon of the TVA-mCherry expression cassette (Figure 1A; see Experimental Procedures). The new construct CAG-FLEX-TC^{Bright} (for TVA-mCherry^{Bright}) produced 10-fold greater mCherry fluorescence in cultured HEK293 cells compared with the original EF1a-FLEX-TC (Figure 1A). We also made similar modifications to the RG-expressing vector and produced CAG-FLEX-RG in AAV2 (AAV serotype 2). For in vivo test, a 1:1 mixture of CAG-FLEX-TC^B

and CAG-FLEX-RG was introduced into the motor cortex of wild-type (negative controls) or *Pvalb*^{Cre/+} knockin (Hippenmeyer et al., 2005) mice. The EnvA-pseudotyped RV (RV- Δ G-GFP+EnvA) was introduced into the same location 2 weeks later, and animals were sacrificed for analysis 4 days afterward. In the *Pvalb*^{Cre/+} mice, we found 811 ± 324 (mean \pm SEM, $n = 3$ animals) mCherry+/GFP+ starter cells clearly labeled with mCherry near the injection site (Figures 1B and 1E). Consistent with results from a previous study (Miyamichi et al., 2011), thousands of mCherry-/GFP+ cells (GFP+ cells in short hereafter) were found near the injection site. Further away from the injection site, we found GFP+ cells in locations consistent with known long-range presynaptic partners of motor cortex neurons (Figure 1B) (Iriki et al., 1989). However, in the negative control animals that did not express Cre, significant number of GFP+ cells (74 ± 30 , $n = 4$ animals), were also present near the injection site (Figure 1C, left), as was reported by Watabe-Uchida et al. (2012). The Cre-independent labeling was restricted to within $\sim 500 \mu\text{m}$ of the injection site and not present in long-range connections; this is likely caused by Cre-independent expression of TVA (see below), as TVA is known to be highly sensitive to EnvA-pseudotyped virus (Wall et al., 2010). Leaky TVA expression also produced local background RV infection when using the tTA/TRE strategy (Miyamichi et al., 2011; Figure S1A available online). As leaky expression of RG is unlikely sufficient to reconstitute infectious RV particles, this does not compromise long-distance tracing of presynaptic partners. However, local GFP+ cells produced by direct infection of Cre-negative cells by RV- Δ G-GFP+EnvA as a result of leaky TVA expression cannot be distinguished from transsynaptic spread from starter cells to local presynaptic partners, compromising specificity of local transsynaptic tracing.

To decrease TVA activity without affecting the expression level of the TVA-mCherry fusion protein, we introduced a point mutation (Glu⁶⁶ \rightarrow Thr, or 66T) in the TVA receptor known to reduce EnvA-enveloped viral transduction by ~ 10 -fold in a cell culture assay (Rong et al., 1998). The expression levels of CAG-FLEX-TC^{66T} and CAG-FLEX-TC^B were comparable in HEK293 cells, as assayed by mCherry fluorescence intensity (Figure 1A). When CAG-FLEX-TC^{66T} was used instead of CAG-FLEX-TC^B along with CAG-FLEX-RG, followed by RV- Δ G-GFP+EnvA, Cre-independent labeling of GFP in the negative control animals was drastically reduced in the motor cortex (0.5 ± 0.5 GFP+ cells, $n = 4$ animals; Figure 1C, right) and in the OB (0.8 ± 0.5 GFP+ cells, $n = 6$ animals) of wild-type CD1 mice that did not express Cre (see Figure S1 for more controls). By contrast, when CAG-FLEX-TC^{66T} and CAG-FLEX-RG were introduced into the motor cortex of *Pvalb*^{Cre/+} mice, we found 36 ± 20 ($n = 4$ animals) mCherry+/GFP+ starter cells clearly labeled with mCherry near the injection site. As expected, hundreds of local GFP+ cells were labeled near the injection site (Figure 1D), although the convergence index (defined as the number of presynaptic GFP+ cells divided by the number of starter cells) for long-distance transsynaptic labeling was significantly lower than those obtained by using CAG-FLEX-TC^B (Figure 1E).

In summary, both CAG-FLEX-TC^B and CAG-FLEX-TC^{66T} allowed transsynaptic tracing and unequivocal labeling of starter cells with the mCherry marker. TC^B is suitable for efficient

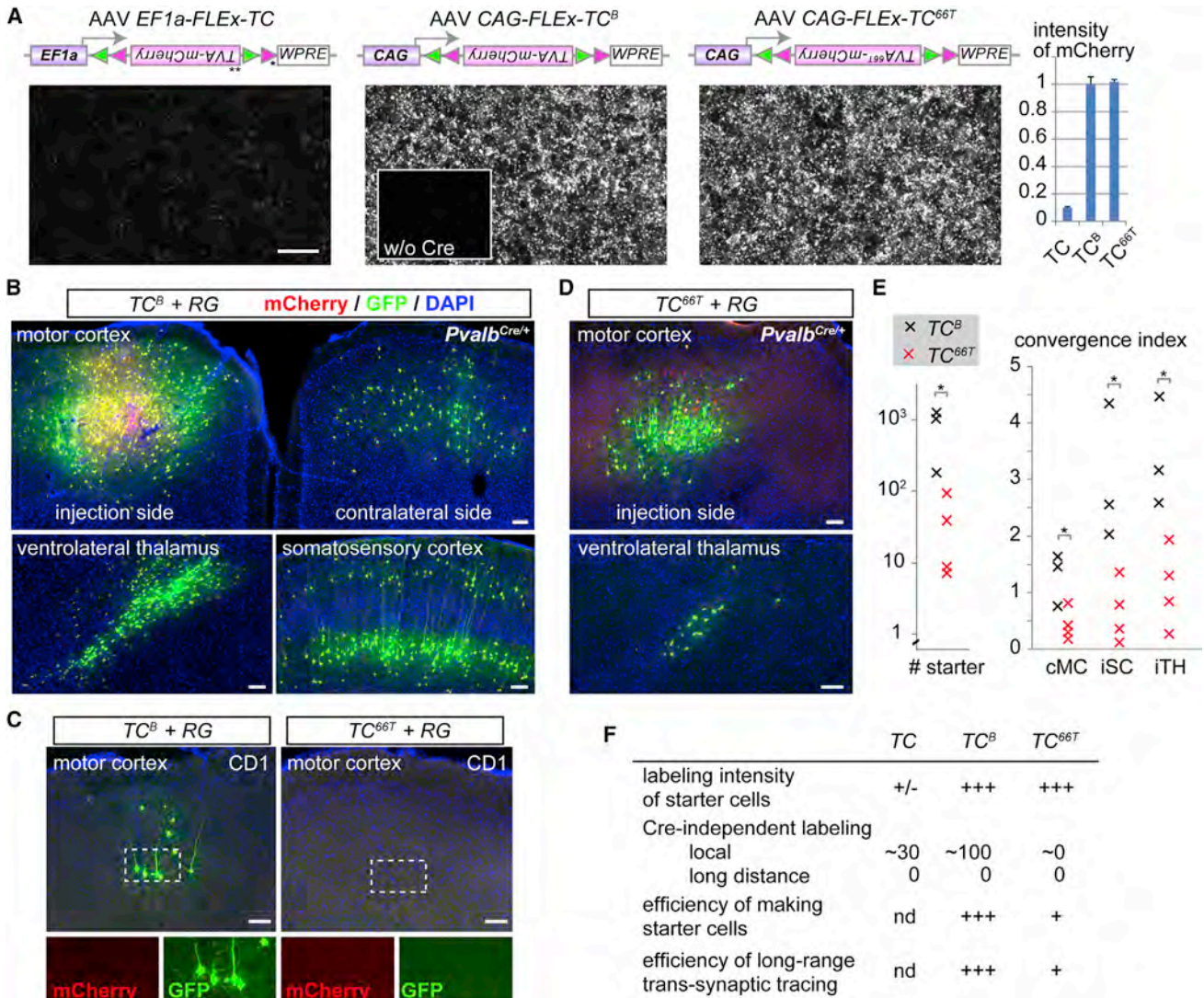


Figure 1. Optimizing Cell-Type-Specific Transsynaptic Tracing

(A) Schematic of the construct and DNA transfection in cultured HEK293 cells. To increase the expression level of Cre-dependent *pEF1a-FLEX-TC* (Watabe-Uchida et al., 2012) (left), we changed the promoter to CAG, removed an upstream and out-of-frame ATG (*) between the promoter and the open reading frame after Cre-mediated recombination and added a Kozak sequence before the start codon (**) for optimal translation (Kozak, 1987). The resultant cassette (*pCAG-FLEX-TC^B*, middle) was further modified by introducing a point mutation in TVA to construct *pCAG-FLEX-TC^{66T}* (right). All constructs, when cotransfected with a CAG-Cre plasmid, allowed 293 cells to express mCherry, while mCherry was not expressed in the absence of Cre (middle inset and data not shown). mCherry expression level was markedly increased in *CAG-FLEX-TC^B* and *CAG-FLEX-TC^{66T}*, as quantified in the right graph (mean ± SEM); mCherry intensity of *CAG-FLEX-TC^B* is normalized to 1.

(B) Proof-of-principle demonstration of Cre-dependent transsynaptic tracing by transducing a mixture of two AAV2 vectors containing *CAG-FLEX-RG* and *CAG-FLEX-TC^B* into the primary motor cortex (M1) of *Pvalb^{Cre/+}* mice, followed by *RV-ΔG-GFP+EnvA*. Starter cells (yellow) and AAV-transduced cells that did not receive RV (red) were restricted to the injection site, and transsynaptically labeled GFP+ neurons (green) were found in presynaptic areas of the M1, including the contralateral M1 (cMC), ipsilateral somatosensory cortex (iSC), and ipsilateral ventrolateral thalamus (iTH).

(C) Negative controls cotransducing AAV2 *CAG-FLEX-TC^B* or *CAG-FLEX-TC^{66T}* with AAV2 *CAG-FLEX-RG* into CD1 mice with no Cre expression. mCherry from AAV was rarely detected, but GFP from RV was detected near the injection site when *CAG-FLEX-TC^B* was used. In contrast, no GFP or mCherry was detected when *CAG-FLEX-TC^{66T}* was used.

(D) A proof-of-principle demonstration of transsynaptic tracing by transducing *Pvalb^{Cre/+}* mice with AAV2 *CAG-FLEX-TC^{66T}* and AAV2 *CAG-FLEX-RG*. Similar to (B), starter cells in M1 and local and long-range presynaptic partners were detected.

(E) Quantification of number of starter cells (left) and convergence index for long-distance tracing. Each “x” represents an individual experiment with *CAG-FLEX-TC^B* (black) or *CAG-FLEX-TC^{66T}* (red). cMC, contralateral motor cortex; iSC, ipsilateral somatosensory cortex; iTH, ipsilateral thalamus.

(F) Summary of three variants of transsynaptic tracing.

Scale bars, 100 μm. See Figure S1 for additional controls and quantification.

long-distance tracing but cannot be used for mapping local circuits near the injection site due to high Cre-independent transduction by EnvA-pseudotyped RV. By contrast, TC^{66T} is suitable for analyzing local circuits with near-zero Cre-independent transduction of EnvA-pseudotyped RV, albeit with reduced number of starter cells (Figures 1E and 1F).

Parvalbumin Neurons Features Prominently in the Presynaptic Landscape of Mitral/Tufted Cells

We next applied $CAG-FLEX-TC^{66T}$ -based transsynaptic tracing to map the presynaptic partners of M/T cells in the OB. We used $Pcdh21-Cre$ mice (Nagai et al., 2005) to restrict starter cells to M/T cells. We targeted M/T cells of the ventrolateral OB (1.6 mm from the dorsal surface). All starter cells (mCherry+/GFP+) in four animals were located either in the superficial layer between glomeruli and the external plexiform layer (EPL; 23 ± 12), or in the mitral cell layer (MCL; 23 ± 11) (Figure 2A), consistent with both the distribution of external tufted cells (eTs) or mitral cells (MCs) and with the expression pattern of $Pcdh21-Cre$. We found $1,997 \pm 588$ mCherry-/GFP+ (hereafter GFP+ cells), presumed presynaptic partners of the starter M/T cells, located in different layers in the OB, including 362 ± 80 periglomerular and external tufted cells in the glomerular layer, 946 ± 261 cells in the EPL, 107 ± 41 cells in the mitral cell layer, 324 ± 159 granule cells, and 259 ± 64 deep short axons cells (dSACs) in the granule cell layer (Figures 2A and 2B). In addition, we detected 218 ± 82 presumed cortical feedback projection neurons in the anterior olfactory nucleus (AON) and anterior piriform cortex (APC; Figures S6D–S6G), two cortical targets of M/T cells.

Among the different cell types labeled in the OB, the most prominent population was located in the EPL with a star-like shape, suggesting an interneuron identity (Kosaka et al., 1994). To characterize the cell types of these GFP+ cells, we costained the OB sections with antibodies against calretinin, calbindin, parvalbumin (PV), tyrosine hydroxylase, and Tbr2. Among the antibodies used, anti-PV antibodies most frequently colabeled GFP+ neurons in the EPL (Figure 2B). Indeed, $88.1\% \pm 1.6\%$ of GFP+ cells in the EPL were PV+ neurons (PVNs) ($n = 3$ animals). To test whether this enrichment reflects connection specificity or bias of RV infection, we directly injected RV carrying its own glycoprotein in its envelope (RV- $\Delta G-GFP+RG$) into the OB, which should transduce all cell types capable of receiving RV whether or not they are synaptically connected with M/T cells. We found that only $33.0\% \pm 1.6\%$ of GFP+ cells in the EPL were PVNs ($n = 3$ animals; Figure S1D). Thus, the enrichment of PVNs in the M/T transsynaptic tracing experiment reflects connection specificity: PVNs are prominent presynaptic partners of M/T cells.

To compare the distribution of labeled cells in different layers and of different cell types across samples, we mapped them to a common 3D reference OB using a modified 3D reconstruction protocol (Miyamichi et al., 2011) (see Supplemental Experimental Procedures and Figure S2). As an example, Figure 2C (top) shows the lateral view of a representative OB sample (same as Figure 2A), with 31 eTs and 27 MCs starter cells (shown in yellow). A distribution of the 1,234 GFP+ PVNs in the EPL (PVNs^{EPL}) are shown in magenta. Interestingly, GFP+ PVNs^{EPL} were more broadly distributed across the OB surface than their

postsynaptic M/T starter cells (see Figure S2D for an additional example). To quantify this observation, we introduced a cylindrical coordinate system into the OB model, where Z represents the position along the anterior-posterior axis and θ represents the angle from the dorsal polar axis (Figure 2C). We normalized individual samples to a common frame and use θ' and Z' to represent normalized values (see Supplemental Experimental Procedures). The histograms in Figure 2D show that PVNs^{EPL} were significantly more widely distributed than their target M/T cells in both axes (Levene's test for equal variance; $p < 0.001$). Notably, longer survival period for RV to spread and label presynaptic neurons did not change tracing efficiency of local circuits or general labeling patterns in the OB (Figure S3). Thus, M/T cells receive input from PVNs that are more broadly distributed spatially than the M/T cells themselves.

Two-Photon-Targeted Patch of PVNs^{EPL} in the Mouse OB

Given that PVNs^{EPL} are prominent presynaptic partners of M/T cells, we next combined mouse genetics with imaging and physiology to determine their odor response properties in vivo. To visualize PVNs, we produced mice carrying $Pvalb^{Cre/+}$ and a Cre-dependent tdTomato reporter (Hippenmeyer et al., 2005; Madisen et al., 2010). As expected from known distributions of PVNs in the OB, tdTomato+ cells were found predominantly in the EPL, with small numbers in the glomerular layer (GL) and granule cell layer (GCL) (Figure 3A). While not all PV+ EPL cells were tdTomato+, the vast majority of EPL tdTomato+ cells were PV+ as assessed by immunostaining (97.2%, $n = 280$ cells from 2 mice; Figure 3B). Therefore, we regard tdTomato+ neurons in the EPL of these mice as PVNs^{EPL}. We targeted PVNs^{EPL} by combining in vivo two-photon imaging of the dorsal surface of the OB with loose-patch recordings (Figure 3C) (Margrie et al., 2003). Unlike in the cortex, where PVNs are known to be fast-spiking interneurons, PVNs^{EPL} in the OB did not have a unique spike shape by which we can validate correct targeting (Figure S4). To validate correct targeting, therefore, we filled each cell with electrode dye after recording (Figure 3D). Only neurons that were successfully patched, recorded throughout the session, and double labeled with tdTomato and the electrode dye were included in our data set.

PVNs^{EPL} Are Broadly Tuned to Odors

We monitored both the spontaneous and odor-evoked activity of PVNs^{EPL} in anesthetized, freely breathing mice ($n = 30$ cells from 15 mice). Spontaneous firing rates of PVNs^{EPL} were highly heterogeneous, spanning between 0.4 and 42 Hz (mean 13.57 ± 1.81 Hz). Furthermore, 90% of PVNs^{EPL} were spontaneously tuned to the phase of the respiratory cycle, with the activity in most cells locked to the inhalation period (binomial proportion test; $p < 0.001$; Figure S4). For odor stimulation, we used a panel of five monomolecular odors known to activate the dorsal OB. A representative example of one such recording in response to a 2 s odor stimulus is shown in Figure 3E. Here, the PVN^{EPL} responded significantly to each of the five odors (paired t test; $p < 0.001$ for all odors).

We recorded the odor response profiles of PVNs^{EPL} as well as two additional neuronal populations in the same mice. One

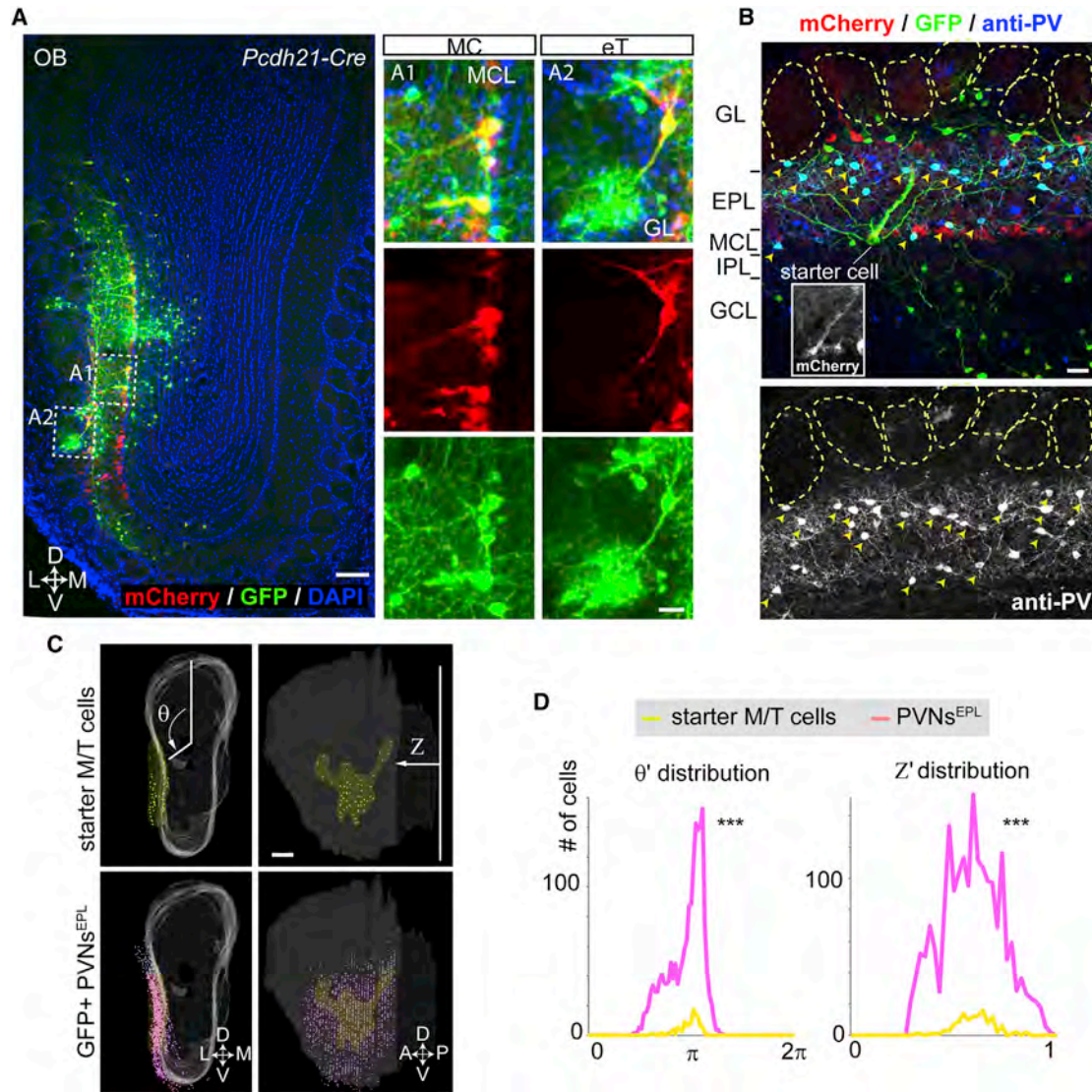


Figure 2. Parvalbumin Neurons in the External Plexiform Layer Are Prominent Presynaptic Partners of M/T Cells

(A) Starter cells were limited to the mitral and tufted cell populations by transducing *Pcdh21-Cre* mice with AAV2 *CAG-FLEX-RG* and AAV2 *CAG-FLEX-TC^{66T}* followed by RV- ΔG -GFP+EnvA. In this 60 μ m coronal section, starter cells are located in the mitral cell layer (MCL) and the boundary between glomeruli and external plexiform layer (eT, for external tufted cells). L, lateral; M, medial; D, dorsal; V, ventral. Scale bars, 100 μ m for the low-magnification image; 20 μ m for the high-magnification images.

(B) A typical example of a 60 μ m coronal section containing a starter MC (inset) and GFP+ presynaptic neurons stained by anti-PV antibodies. GL, glomerular layer; EPL, external plexiform layer; MCL, mitral cell layer; IPL, internal plexiform layer; GCL, granule cell layer. Neurons colabeled with GFP and anti-PV antibodies are indicated by yellow arrowheads. Scale bar, 20 μ m.

(C) A representative example of 3D-reconstructed OB showing starter M/T cell populations (yellow dots) and GFP+ PVNs^{EPL} (magenta dots). White shadow represents the 2D surface of the MCL in the 3D OB model. θ represents rotation angle from the polar axis (vertical line in the left top), and Z represents the relative distance from the most posterior section. A, anterior; P, posterior. Scale bar, 200 μ m.

(D) Histograms showing distribution of normalized θ and Z (θ' and Z') for pooled data (n = 3 mice). Notably, both θ' and Z' distribution of PVNs^{EPL} was significantly broader than those of starter cells. Statistical significance was tested by the Levene's test against the null hypothesis assuming equal variance between two populations (***p < 0.001).

See Figure S2 for 3D reconstruction of labeled OB samples, Figure S3 for tracing with a longer survival period after RV infection, and Figure S6 for cortical feedback input to M/T cells.

additional group was comprised of tdTomato-negative cells in the EPL (n = 20 cells, from 11 mice). Although little is known about these cells, previous studies showed that they include interneurons expressing somatostatin, CRH, calretinin, or TH

alone or in combination, as well as tufted cells (Hamilton et al., 2005; Huang et al., 2013). Based on our estimation that PV+ cells comprise 33% of the EPL cells (Figure S1D), and as only 24% of PV+ neurons did not express tdTomato (Figure 3B), we infer that

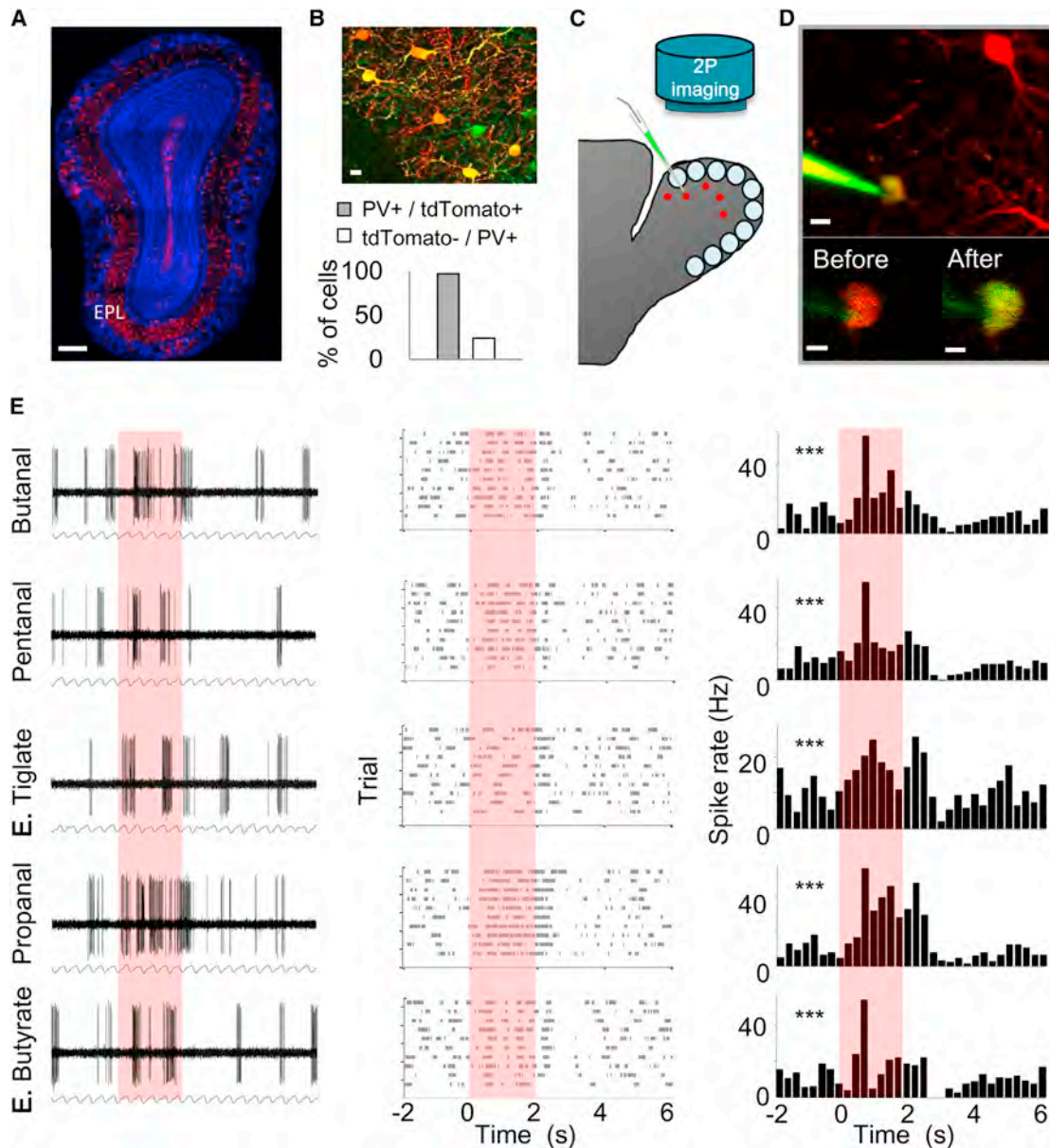


Figure 3. Two-Photon-Targeted Recording of OB PVNs In Vivo

(A) A confocal micrograph of an OB coronal section from a *Pvalb^{Cre/+}; Rosa26^{Ai9/+}* mouse, showing conditional expression of tdTomato in PVNs (red). EPL, external plexiform layer. Scale bar, 250 μ m.

(B) Top: a merged image of PV immunostaining (green) and tdTomato expression (red). Yellow cells denote double labeling. Scale bar, 15 μ m. Bottom: in the EPL, $P(\text{PV+}/\text{tdTomato+})$ is 97.2%, and $P(\text{tdTomato-}/\text{PV+})$ is 24.0% ($n = 280$ cells from two mice). Based on our estimate that one-third of EPL cells are PV+ (Figure S1D), we infer using Bayes' rule that $P(\text{PV+}/\text{tdTomato-})$ is $\sim 11\%$.

(C) Schematic of two-photon-targeted patch (TTP) recording from PV+ neurons.

(D) Top: a two-photon micrograph showing an in vivo TTP recording from a $\text{PVN}^{\text{EPL+}}$ neuron. Scale bar, 10 μ m. Bottom: two-photon micrograph of the cell body before (left) and after (right) recording. Yellow somata denote successful labeling. Scale bar, 5 μ m.

(E) Representative example of a loose-patch recording from a PVN^{EPL} presented with five odors. Each row represents the responses to a single odor; red box indicates odor presentation (2 s). Left: raw voltage traces showing spontaneous and odor-evoked activity during one trial. The respiration trace is shown below. Middle: raster plots showing spontaneous and odor-evoked activity across all trials. Right: peristimulus time histogram (PSTH) showing average spike rates across trials (binning 250 ms). Asterisks mark significant responses (paired t test; $***p < 0.001$).

See Figure S4 for spontaneous electrophysiological properties of PVN^{EPL} .

tdTomato-negative cells expressing PV+ comprise only ~11% of the EPL. Thus, we collectively refer to tdTomato-negative cells in the EPL as non-PVNs^{EPL}. The second interneuron group we used for comparison was the GCs, the largest interneuron population in the OB ($n = 27$ cells, from 4 mice). Recordings from PVNs^{EPL} and non-PVNs^{EPL} were made strictly from the EPL (mean recording depth $186.76 \pm 42.13 \mu\text{m}$) using two-photon-targeted patch, and GCs were targeted blindly by limiting the pipette depth to the GCL ($>340 \mu\text{m}$; Figure 4A). Additionally, non-PVNs^{EPL} were filled with dye after recording to verify that the recording was from an EPL cell body, rather than an en passant neurite (Figure 4B). This preparation allowed us to perform the first in vivo functional investigation of sparse, genetically defined subpopulations in the OB.

Recording the odor-evoked activity of these three groups allowed us to compare their odor response profiles under similar conditions. We first examined the odor selectivity of each group by testing each cell's spiking response to the panel of five odors. Neurons that responded to all five odors were considered nonselective or broadly tuned (see Experimental Procedures). Our first striking observation was that PVNs^{EPL} were particularly broadly tuned. For example, Figure 4C shows three PVNs^{EPL} responding to three, four, or all five odorants (Figure 4C, asterisks). In contrast, non-PVNs^{EPL} and GCs normally responded to only one to two odors (Figures 4D and 4E, asterisks). In total, while 93% (28/30 neurons) of the PVNs^{EPL} responded to three or more odors, only 25% (5/20 neurons) of the non-PVNs^{EPL} and 11% (5/27 neurons) of the GCs responded similarly (Figure 4F). Moreover, 33% (10/30 neurons) of the PVNs^{EPL} responded to all odors presented, whereas none of the GC and only 5% (1/20 neurons) of the non-PVNs^{EPL} showed such broad tuning (Figure 4F). Statistical analysis validated that the PVNs^{EPL} were significantly more broadly tuned to odors compared to the two other populations we tested (Tukey's HSD, $p < 0.05$, Figure 4F).

Unique Odor Response Profile of PVNs^{EPL}

Having found that PVNs^{EPL} are particularly broadly tuned to odors, we next analyzed whether they have other unique physiological properties. We first subdivided odor responses into changes in firing rates and in phase tuning (see Experimental Procedures). While PVNs^{EPL} showed both types of odor-evoked responses (e.g., Figure 5A for rate changes; Figures 5B and 5C for phase tuning changes), the vast majority of odor responses were characterized by changes in firing rate ($>95\%$, binomial test; $p < 0.001$, Figure 5D). Odor-evoked changes in PVNs^{EPL} firing rate were primarily excitatory (Figures 5A₁–5A₃ and 5E), but some neurons showed inhibitory responses (Figure 5A₄). Interestingly, most PVNs^{EPL} ($>80\%$) and non-PVNs^{EPL} exhibited either exclusively excitatory or exclusively inhibitory odor-evoked responses. By contrast, GCs showed similar levels of excitatory and inhibitory responses, even within a given cell (Figure 5E; Figure S5). These data suggest that PVNs^{EPL} receive predominantly excitatory (or disinhibitory) inputs.

To further examine the physiological characteristics of PVNs^{EPL}, we classified excitatory odor responses into three categories: "on," "persistent," and "off" responses. Examples of all three response types from different PVNs^{EPL} are shown in Figures 5A₁–5A₃. All three groups showed predominantly "on"

responses (89%, 85%, and 87% for PVN^{EPL}, non-PVN^{EPL}, and GC, respectively; Figure 5F). Interestingly, however, and unique to PVNs^{EPL}, over 40% of excitatory responses persisted after odor stimulation had ended (mean persistent response to a 2 s odor stimulation was 7.13 ± 0.38 s). Finally, the magnitude of PVNs^{EPL} responses (quantified by the absolute maximal changes in firing rates) was significantly higher than that of both non-PVNs^{EPL} and GCs (Tukey's HSD, $p < 0.05$, Figure 5G). Taken together, these data suggest that PVNs^{EPL} exert robust and persistent inhibition upon M/T cells to a wide range of stimuli.

PVNs Integrate Input from Broadly Distributed Mitral/Tufted Cells

To investigate the underlying basis for the broad odor tuning of PVNs^{EPL}, we applied the *CAG-FLEX-TC^{66T}*-based transsynaptic tracing strategy using *Pvalb^{Cre/+}* mice (Hippenmeyer et al., 2005) to determine the presynaptic landscape of the PVNs themselves ($n = 7$ mice). Almost all ($>97\%$) starter cells (mCherry+/GFP+) were clearly labeled with PV antibodies (Figure 6A). As expected from previous anatomical studies, in addition to the PVNs^{EPL}, starter cells were often found in the deeper internal plexiform and granule cell layers (IPL/GCL; Figure 6A; hereafter referred to as PVNs^{IPL}). On average, we detected 11.7 ± 3.7 starter PVNs and various types of GFP+ neurons in the OB (271.6 ± 83.9 cells per animal) and in the AON/APC (76.9 ± 48.5 cells; Figures S6A–S6C), which are presumed presynaptic partners of PVNs. GFP+ neurons in the OB included periglomerular and external tufted cells in the glomerular layer (29.4 ± 6.9 cells), EPL neurons (90.1 ± 39.2 cells), MCs (43.0 ± 10.8 cells), granule cells (5.9 ± 1.8 cells), and dSACs (106 ± 33.9 cells). In two samples, we obtained exclusively PVNs^{EPL} as starter cells. In both samples, MCs were detected as presynaptic partners, indicating MC→PVN^{EPL} direct connections. The convergence index was 7.8 and 6.3, indicating that multiple MC inputs converge onto each PVN^{EPL}. As noted previously (Marshall et al., 2010; Miyamichi et al., 2011), convergence index derived from RV-based transsynaptic tracing is probably an underestimate of the real connectivity.

We next analyzed the spatial distribution of neurons presynaptic to PVNs using 3D-reconstructed OBs. Figure 6B shows a representative example (animal 1) with starter PVNs exclusively in the EPL restricted to the region near the injection site. Presynaptic partners to these PVN^{EPL} starter cells were more widely distributed spatially than the PVN^{EPL} starter cells themselves. Notably, the presynaptic MCs (shown in red) were located most broadly, both along the dorsal-ventral and anterior-posterior axes. Other examples (that contained both PVN^{EPL} and PVN^{IPL} as starter cells) showed a similar trend. The histograms of θ' and Z' (Figure 6C, $n = 7$ pooled data) showed that presynaptic MCs were significantly more broadly distributed compared to the starter PVNs along both the dorsal-ventral axis (θ') and the anterior-posterior axis (Z') (Levene's test for equal variance; $p < 0.01$). The combined data of presynaptic partner tracing from the M/T (Figure 2) or the PV (Figure 6) cells as starter cells revealed reciprocal connectivity in the form of MC→PVN^{EPL}→MC. In this feedback loop, individual M/T cells on average labeled 16.7 input PVNs^{EPL}, each of which labeled ~7 input MC cells. Thus, even taking into consideration that the

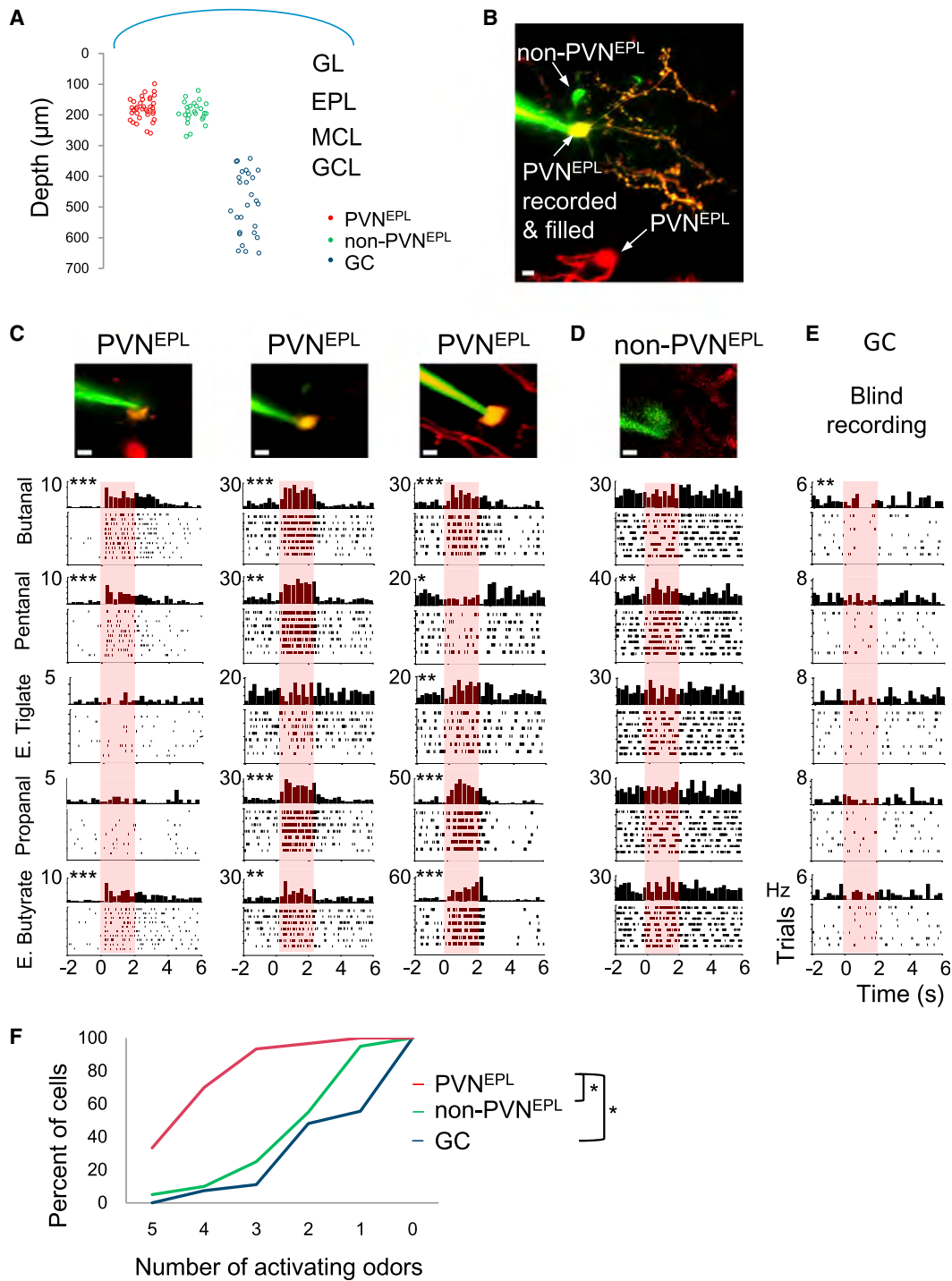


Figure 4. PVNs Are Broadly Tuned to Odors

(A) Distribution of the depth of recording of all neurons in our data set.

(B) A two-photon micrograph of a nonrecorded PVN^{EPL} (tdTomato only, red), a PVN^{EPL} that was recorded from (TdTomato and dye, yellow) and a non-PVN^{EPL} (dye only, green). Scale bar, 10 μm.

(C–E) Neuronal responses from three PVN^{EPL} (C), one non-PVN^{EPL} (D), and one granule cell (GC) (E). PSTHs and raster plots showing odor-evoked responses (or lack thereof) to five odors. Asterisks mark significant responses **p* < 0.05; ***p* < 0.01; ****p* < 0.001 (paired t test). The two-photon micrograph of the recorded neuron is shown above. Scale bar, 10 μm.

(F) Cumulative distribution plot of odor selectivity in response to five odors for PVN^{EPL} (n = 30 neurons, red), non-PVN^{EPL} (n = 20 neurons, green), and GCs (n = 27 neurons, blue). Tukey's HSD; **p* < 0.05.

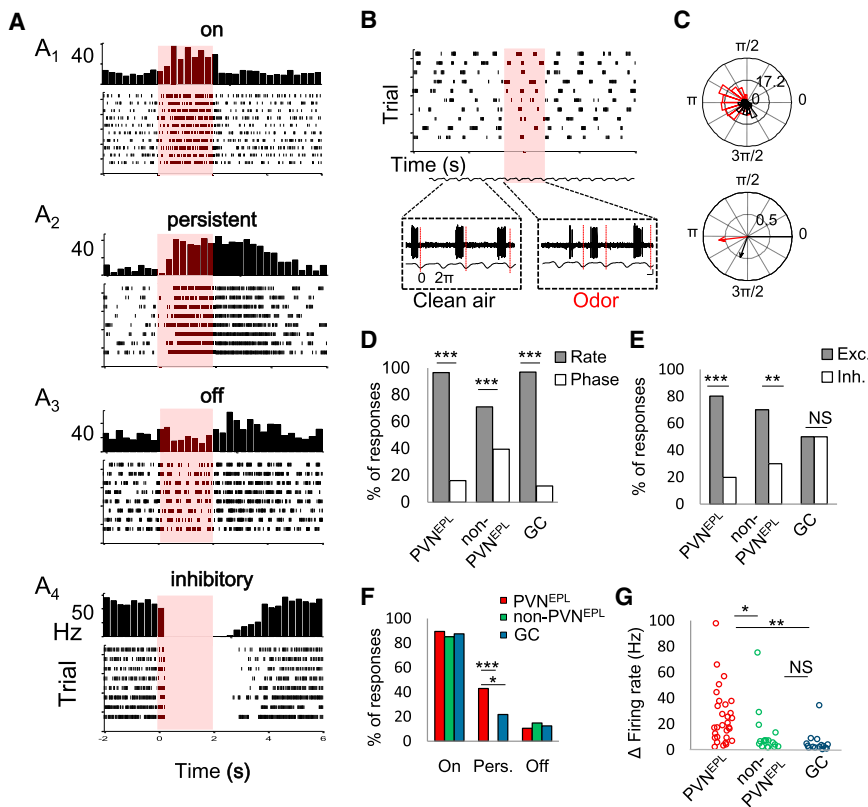


Figure 5. Odor Response Profiles of PVNs Are Predominantly Excitatory

(A) Examples (PSTHs and raster plots) of four types of responses in PVN^{EPL} neurons: on (A₁), persistent (A₂), off (A₃), and inhibitory (A₄). Each panel is a different cell and odor pair.

(B) An example of an odor-evoked response by phase tuning in a PVN^{EPL} neuron. Top: raster plot for a single odor (eight trials). Bottom: raw spiking traces with regard to the respiration before and during odor presentation.

(C) Phase analysis of the cell shown in (B). Top: binned data of spike respiration phase tuning across all trials before and during odor presentation (black and red, respectively). Bottom: direction and magnitude of the mean resultant phase tuning vector before and during odor stimulation.

(D) Histogram of odor-evoked changes in firing rate and odor-evoked changes in phase tuning for all cell groups (binomial proportion test; $p < 0.001$).

(E) Histogram of odor-evoked excitatory versus inhibitory responses for each group (binomial proportion test; $p < 0.01$).

(F) Histogram of the percentage of on, persistent (pers.), and off odor-evoked responses for each group (binomial proportion test; $p < 0.05$).

(G) Response magnitude of odor-evoked changes in firing rate for each group (Tukey's HSD, $p < 0.05$). In (D)–(G), * $p < 0.05$; ** $p < 0.01$; *** $p < 0.001$. NS, not significant.

See Figure S5 for distribution of cells that exhibit excitatory, inhibitory, or both excitatory and inhibitory responses among PVNs^{EPL}, non-PVNs^{EPL}, and GCs.

convergence index from RV-based transsynaptic tracing reflects a lower bound, individual M/T cells disynaptically communicate with >100 M/T cells that are broadly spread in the OB via PVNs as intermediate neurons (Figure 8).

Mitral Cell-Granule Cell Reciprocal Connections Are Narrowly Organized

GCs are known to receive excitatory input from MC's secondary dendrites in the EPL and send back inhibitory output to the dendrites of parent and nearby MCs (Shepherd, 2004). This MC→GC→MC feedback loop is thought to mediate recurrent and lateral inhibition. However, in vivo evidence to support these models is still limited, and the spatial distribution of this lateral connectivity is unknown. To investigate the circuit organization of MC-GC connections in comparison to the MC→PVN^{EPL}→MC feedback loop, we used transsynaptic tracing. It is challenging to restrict starter cells to GCs, however, because GC-specific Cre driver lines have not been reported. Instead, we used a pan-GABAergic driver, *GAD2^{Cre/+}* (Taniguchi et al., 2011), and injected Cre-dependent AAVs (*CAG-FLEX-TC^{66T}* and *CAG-FLEX-RG*) into the GCL of the OB, taking advantage of the fact that the vast majority GCL neurons are GCs. We obtained two samples (out of eight OBs injected and analyzed) that contained starter cells only in the GCL, without “contamination” of periglomerular cells, EPL neurons, or dSACs. In one sample (Figure 7A), 82 starter GCs produced 272 presynaptic GFP+ neurons in the OB. In contrast to the neuronal populations

presynaptic to M/T cells or PVNs, no neurons in the glomerular layer or external tufted cells were labeled from starter GCs. From the pooled data of both samples, a single starter GC, on average, labeled 0.54 MCs, 0.87 EPL neurons, 0.57 dSACs, and 0.6 pyramidal cells in the AON/APC (Figure S6G). To quantitatively analyze the spatial distribution of presynaptic MCs relative to the starter GCs, we reconstructed the OB as shown above (Figures 7B and 7D, top). MCs that were presynaptic to GCs formed clusters close to the starter cells without significant lateral spread. This distribution of presynaptic MCs was in sharp contrast to the widespread distribution M/T cells presynaptic to PVNs (Figures 6B and 6C).

Finally, we analyzed the spatial organization of GC→MC connections from the transsynaptic tracing data using *Pcdh21-Cre* (Figure 2). The distribution of presynaptic GCs (Figure 7C, green) was only slightly greater than the area of the starter MCs (Figure 7C, yellow). Pooled and normalized distributions (θ' and Z') supported this observation quantitatively (Figure 7D, bottom). Thus, the projection neurons of the OB, the mitral/tufted cells, are connected to two local feedback loops involving PVNs^{EPL} and GCs, with striking differences in their physiological properties (Figures 4 and 5) and anatomical organization (Figures 2, 6, and 7).

DISCUSSION

Here, we used cell-type-specific transsynaptic tracing and in vivo physiology to characterize the circuit composed of the reciprocal

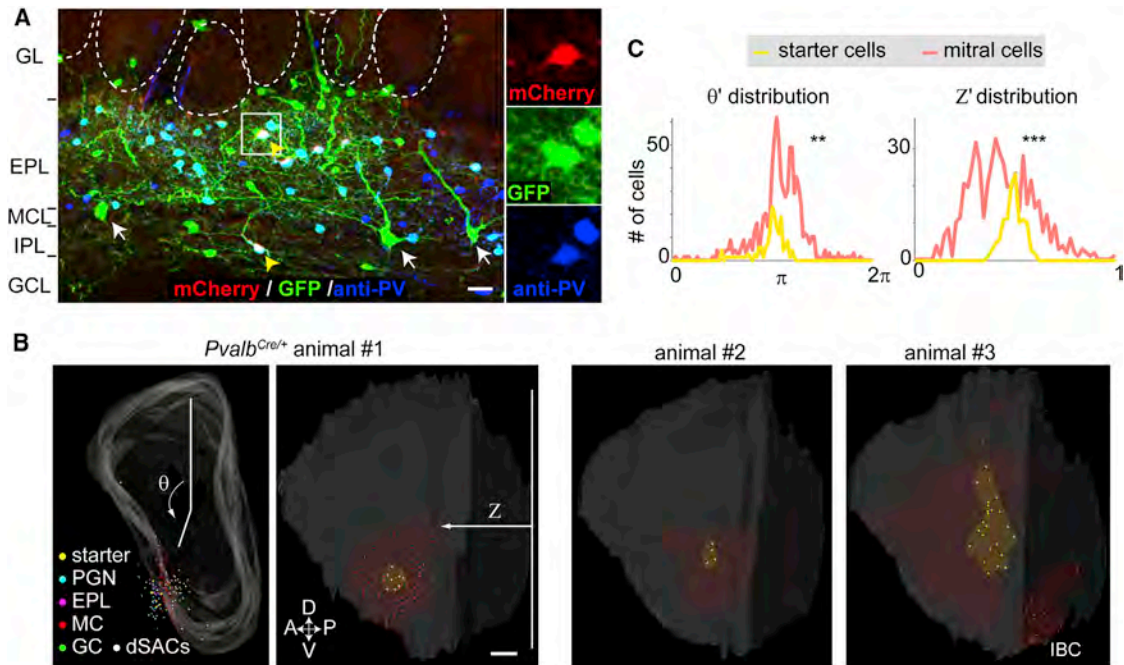


Figure 6. The Presynaptic Landscape of PVNs Includes Widely Distributed MCs

(A) A representative 60 μm coronal section with starter cells costained with anti-PV antibodies. In this section, two PV+ starter cells were detected, one each in the EPL and IPL (yellow arrowheads). White arrows represent mitral cells. Abbreviations are as in Figure 2B. Scale bar, 20 μm .

(B) Three representative examples of 3D-reconstructed OBs showing starter PVNs (yellow dots) and GFP+ presynaptic neurons in the frontal (animal 1, left) and lateral (the rest) views. Different cell type/layer is represented by differently colored dots. Area of starter cells and MCs are highlighted by yellow and red shadows. θ and Z are as in Figure 2. Note that some samples (for example, animal 3) contain labeled MCs in the mirror imaged area of the injection site (IBC, intrabulbar connections) (Schoenfeld et al., 1985). Scale bar, 200 μm .

(C) Histograms showing distribution of normalized θ' and Z (θ' and Z') for pooled data ($n = 7$ mice). Notably, both θ' and Z' distribution of presynaptically labeled MCs are significantly broader than those of starter cells. ** $p < 0.01$ and *** $p < 0.001$ by the Levene's test against the null hypothesis assuming the equal variance between two populations.

See Figure S6 for cortical feedback input to PVNs.

connections between PVN^{EPL} and M/T cells. We discuss below the anatomical and physiological properties of this circuit in comparison with the $\text{MC} \rightarrow \text{GC} \rightarrow \text{MC}$ circuit and suggest that $\text{M/T} \rightarrow \text{PVN}^{\text{EPL}} \rightarrow \text{M/T}$ connections form a spatially broad lateral inhibitory circuit in the OB (Figure 8). We also discuss the technical advances and limitations of applying transsynaptic tracing tools to untangle the complexity of local neuronal circuits.

In the OB, odor information from sensory neurons is processed by multiple local networks of interneurons. Local networks thus shape the activity of M/T cells that convey odor information to higher brain regions (Dhawale et al., 2010; Kikuta et al., 2013; Tan et al., 2010). The presynaptic landscape of M/T cells described here provides a rudimentary “roadmap,” upon which physiological and functional studies can be integrated for understanding the complex interactions underlying transformations of olfactory information. From this landscape, the PVN^{EPL} subpopulation emerged as a prominent source of M/T cell input (Figure 2). PVNs have recently attracted much attention elsewhere in the brain (Isaacson and Scanziani, 2011; Tiesinga and Sejnowski, 2009). In the cortex, for example, these cells provide classic feedforward inhibition onto pyramidal cells, controlling both the timing and spatial spread of cortical excitation (Cruikshank et al., 2007; Gabernet et al., 2005; Gibson et al.,

1999; Inoue and Imoto, 2006; Poo and Isaacson, 2009). Cortical PVNs have also been implicated in forming gamma oscillations (Sohal et al., 2009), regulating the activation of quiescent hippocampal stem cells (Song et al., 2012) and the onset of developmental critical periods in an experience-dependent manner (Kuhlman et al., 2011). In the OB, the role of PVNs has been inferred largely from anatomical studies, where their connectivity onto M/T cells has been established (Kosaka and Kosaka, 2008, 2011). Here we highlight two prominent features of PVNs^{EPL} : their relatively broad odor tuning and spatially widespread connection patterns. Notably, both of these features are rather unique in comparison to other neurons in the OB (Davison and Katz, 2007; Fantana et al., 2008; Kato et al., 2012; Kikuta et al., 2013). What may be the role of broadly tuned interneurons exerting widespread local inhibition in the OB?

Previous studies examining the inhibition performed in the EPL have largely focused on the $\text{MC} \rightarrow \text{GC} \rightarrow \text{MC}$ circuit. This reciprocal connectivity has been proposed to mediate nearest-neighbor lateral inhibition, as well as recurrent inhibition (Margrie et al., 2001; Mori et al., 1999; Yokoi et al., 1995). More recently, this lateral inhibitory circuit has been suggested to function in a spatially distributed manner, among distinct glomerular units that are not limited to the nearest-neighbor glomeruli

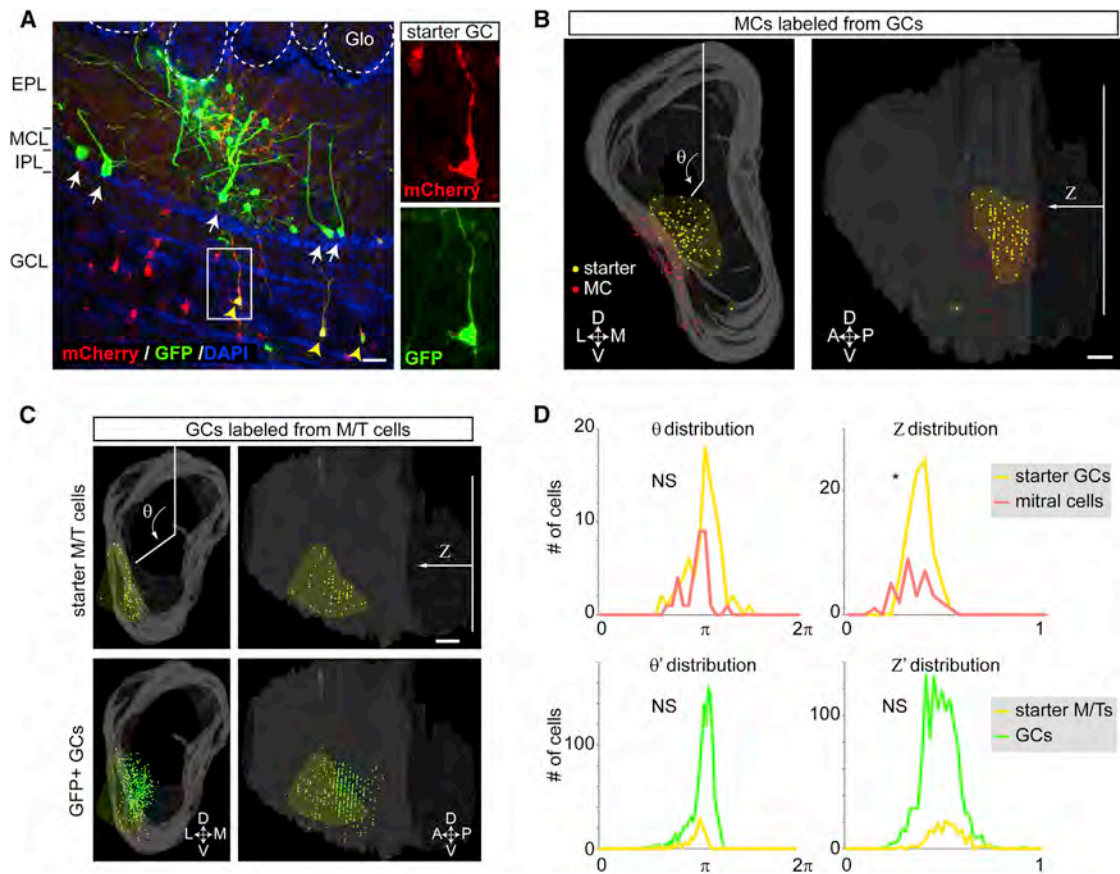


Figure 7. Mitral Cell-Granule Cell Reciprocal Connections Are Narrowly Organized

(A) A representative 60 μm coronal section with starter cells in the granule cell population (yellow arrowheads). Transsynaptically labeled MCs (white arrows) and EPL neurons were labeled with GFP. Abbreviations are as in Figure 2B. Scale bar, 20 μm .

(B) A representative example of 3D-reconstructed OB showing starter GCs (yellow dots) and GFP+ presynaptic MCs (red dots) in the frontal (left) and lateral (right) views. Area of starter cells and MCs are highlighted by yellow and red shadows. θ and Z are as in Figure 2. Scale bar, 200 μm .

(C) A representative example of 3D-reconstructed OB showing starter mitral/tufted (M/T) cells (yellow dots) and GFP+ presynaptic GCs (green dots) in the frontal (left) and lateral (right) views. Areas of starter M/T cells are highlighted by yellow shadows. Scale bar, 200 μm .

(D) Top: histograms showing distribution of θ and Z for the sample shown in (B). The variance of θ for the starter granule cells and presynaptic MCs are not significantly different (NS), while the variance of Z is significantly different ($p < 0.05$). Bottom: histograms showing distribution of normalized and pooled θ and Z (θ' and Z') for the $n = 4$ samples of condition shown in (C). The variance of θ' and Z' for the starter mitral/tufted (M/T) cells and presynaptic granule cell (GCs) are not significantly different (NS) by the Levene's test.

(Debarbieux et al., 2003; Fantana et al., 2008). Our anatomical and physiological data suggest that the GC feedback loop is narrowly tuned both spatially and functionally, supporting their role in local columnar computation. By contrast, the spatially and functionally broad MC \rightarrow PVN^{EPL} \rightarrow MC feedback loop suggests a role in more global computations within the EPL (Figure 8). For example, one computation commonly thought to be performed in the OB is decorrelation of similar odor representations (Cleland, 2010). Although the dominant models of bulbar decorrelation focus on interglomerular mechanisms at the glomerular layer (Aungst et al., 2003; Whitesell et al., 2013) or GC lateral inhibition, broadly tuned inhibition may also provide a complementary mechanism to promote decorrelation (Poo and Isaacson, 2009; Sohya et al., 2007). Specifically in the OB, PVNs^{EPL} would exert robust inhibition onto M/T cells, effectively elevating their response threshold. Additionally, both theoretical

models and experimental observations suggest a role for broadly tuned inhibition in input normalization. In the OB and *Drosophila* antennal lobe (analogous to vertebrate OB), broadly tuned inhibition, scaled by the total input activity, may enable the limited dynamic range of projection neurons to encode information over a wide range of odorant concentration (Isaacson and Scanziani, 2011; Olsen et al., 2010). The inhibition exerted by PVN^{EPL} is broadly distributed across the input field. Thus, these cells may promote the relative, rather than absolute, odor representation by M/T cells (see Kato et al., 2013).

The broad odor tuning of PVNs is consistent with the broad distribution of M/T \rightarrow PVN excitatory inputs, while the narrow responsiveness of GCs can be explained by the narrowly distributed connectivity. How do multiple local feedback circuits operate at distinct spatial scales? One hypothesis is that GCs form reciprocal synapses more preferentially on proximal dendrites

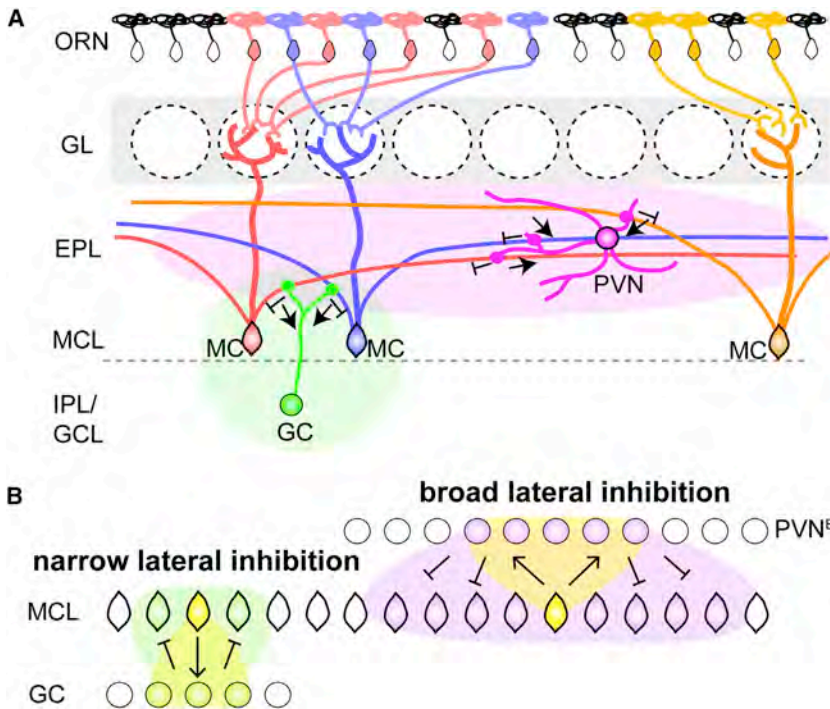


Figure 8. Feedback Circuits by PVNs^{EPL} Underlying Broad Odor Processing

(A) Schematic summary of the MC→PVN^{EPL}→MC circuit in the OB. Each PVN^{EPL} receives input from, and sends output to, broadly distributed MCs via MCs' long secondary dendrites in the EPL for broad lateral inhibition of MC output. In contrast, the MC→GC→MC feedback circuit connects nearby MCs for local lateral inhibition. The green and magenta ovals symbolize areas influenced by PVN and GC.

(B) Schematic illustration of the difference in the spatial spread of the two lateral inhibitory feedback loops.

(closer to the cell bodies), while PVNs^{EPL} do not have such a bias. Indeed, a previous pseudorabies virus-mediated multisynaptic circuit mapping study identified cluster-like organization of the GC-M/T connections (Willhite et al., 2006), consistent with the narrow spatial distribution. Our data suggests that GCs connect predominately near the parent mitral cell soma.

In this study, we improved the RV-based Cre-dependent transsynaptic tracing system (Wall et al., 2010; Watabe-Uchida et al., 2012) (Figure 1), enabling analysis of local connectivity in any circuit with starter cells defined by a specific Cre line. We provided evidence in support of synaptic specificity of RV spread. For example, ~88% of RV labeled neurons in the EPL from the starter M/T cells were PVNs, despite the fact that PVNs constitute only ~33% of all RV-infectable cells in the EPL (Figure S1D). Therefore, selective RV spread from M/T cells to PVNs^{EPL} indicates both strong PVN^{EPL}→M/T connections and preferential RV spread through synaptic connections. External tufted cells were not labeled from starter GCs, despite the fact that their secondary dendrites (Igarashi et al., 2012) are intermingled with the ascending dendrites of GCs, also supporting the synapse specificity of RV spread. Our study also extended the utility of RV tracing to mapping connections made by atypical dendrodendritic connections between M/T and PVNs^{EPL} or GCs (Shepherd et al., 2007), at least qualitatively. However, transsynaptic tracing is still a method under development and its limitations are not fully understood. For example, a major caveat is that only a subset of presynaptic partners of starter cells are labeled, leading to significant underestimation of the full connectivity matrix. Therefore, the quantitative data regarding convergence ratio should only be interpreted in a relative rather than absolute manner. Another limitation of the current study is that we cannot distinguish mitral from tufted

cells, as a mitral cell-specific Cre line has yet to be established. As their electrophysiological properties (Nagayama et al., 2004) and axonal projection patterns (Igarashi et al., 2012) are different, it will be interesting to compare the presynaptic landscape of these two distinct classes of projection neurons in the OB as genetic tools become available in the future. Nevertheless, our approach of integrating cell-type-specific tracing with in vivo physiology facilitates studies of local circuits individually, yet retaining the context of their larger networks. We expect it to be widely applicable to dissect the function of neural circuits in many other parts of the brain.

EXPERIMENTAL PROCEDURES

Animals

All animal procedures followed animal care guidelines approved by Stanford University's Administrative Panel on Laboratory Animal Care (A-PLAC) and the Hebrew University Animal Care and Use Committee. The *Pcdh21-Cre* (Nagai et al., 2005) mouse was obtained from RIKEN Bioresource Center (Japan). *Pvalb^{Cre}* (Hippenmeyer et al., 2005), *GAD2^{Cre}* (Taniguchi et al., 2011), and Cre-dependent tdTomato reporter strain *ROSA26^{tdTomato}* (Madisen et al., 2010) were obtained from the Jackson Laboratories.

Surgical and Viral Procedures

To genetically label PV-positive neurons (Figures 3, 4, and 5), a total of $n = 27$ *Pvalb^{Cre/+}; ROSA26^{tdTomato/+}* double heterozygous mice were used, both male and female, 8–12 weeks old. Twenty-five mice were used for in vivo electrophysiology experiments and two for histology. For electrophysiology, mice were anesthetized with an intraperitoneal injection of ketamine and medetomidine (100 mg/kg and 0.83 mg/kg, respectively) and a subcutaneous injection of carprofen (0.004 mg/g). Additionally, dextrose saline was injected to prevent dehydration. Experiments lasted up to 11 hr (usually ~6 hr). The depth of anesthesia was assessed by monitoring the pinch withdrawal reflex and rectal temperature was continuously monitored and maintained at $36^{\circ}\text{C} \pm 1^{\circ}\text{C}$. For imaging and recording, a craniotomy (~1 × 2 mm) was performed over the OB of one hemisphere, while taking care to ensure that the dura remained intact.

For transsynaptic labeling (Figures 1, 2, 6, and 7), 0.3 μl of 1:1 mixture of AAV *CAG-FLEX-RG* and AAV *CAG-FLEX-TC* (TC^B for the experiments in Figure 1 and TC^{66T} for the experiments in Figures 2, 6, and 7) was injected into the brain at postnatal day (PD) 21 by using a stereotaxic apparatus (KOPF). During surgery, animals were anesthetized with 65 mg/kg ketamine and 13 mg/kg xylazine (Lloid Laboratories). For motor cortex injections, the needle was placed

1.5 mm anterior and 1.5 mm lateral from the bregma and 0.4 mm from the brain surface. For OB injections, needle was placed 4.2 mm anterior and 0.8 mm lateral from the bregma and 1.6 mm from the OB surface. After recovery, animals were housed in regular 12 hr dark/light cycle with food and water ad libitum. Two weeks later, 0.3 μ l of pseudotyped RV (Δ G-GFP+EnvA) was injected into the same brain location under anesthesia. After recovery, animals were housed in a biosafety room for 4 days (or 8 days only for Figure S3) to allow RV to infect, transsynaptically spread, and express sufficient amount of GFP to label presynaptic cells.

Electrophysiology

Imaging was performed on an Ultima two-photon microscope from Prairie Technologies, using a 16 \times water-immersion objective lens (0.8 NA; CF175, Nikon) at 915 nm excitation (DeepSee femtosec laser, Spectraphysics). Electrodes (5–10 M Ω) were filled with an internal solution containing 140 mM K-gluconate, 10 mM KCl, 10 mM HEPES, 10 mM Na₂-Phosphocreatine, 4 mM MgATP, 0.4 mM Na₂GTP, and 0.5 mM EGTA, pH adjusted to 7.25 with KOH. We added 200 μ M Alexa Fluor 488 (Life Technologies, Invitrogen) in targeted recordings, and dye from the electrode was electroporated into the cell using current pulses. Only tdTomato+ cells that were distinctly filled during this procedure were included in our PVN^{EPL} and non-PVN^{EPL} data set.

Odor stimuli were delivered directly to the nose via a custom made 5-channel olfactometer with completely isolated odor channels to circumvent contamination between odors. The odors (Butanal, Pentanal, ethyl tiglate, propanol, and ethyl butyrate) were delivered for 2 s (4–10 trials/odor) in a pseudorandom order, with an interstimulus interval of 18 s at a final concentration of 50 ppm or 500 ppm. No significant differences between the average data of these concentrations were found so data were pooled. The animal's respiration was monitored throughout the experiment by a low pressure sensor (1-INCH-D1-4V-MINI, by "All sensors"), which was used to identify the inhalation onset during the respiratory cycle and to trigger odor delivery. All data analysis was carried out by custom-written MATLAB programs.

Additional procedures on constructs and virus preparations, two-photon-targeted recording from PV-positive neurons, respiration-triggered odor delivery, electrophysiological data analysis, immunohistochemistry and microscopy, and 3D reconstruction and quantitative analysis can be found in the [Supplemental Experimental Procedures](#).

SUPPLEMENTAL INFORMATION

Supplemental Information includes Supplemental Experimental Procedures and six figures and can be found with this article online at <http://dx.doi.org/10.1016/j.neuron.2013.08.027>.

AUTHOR CONTRIBUTIONS

K.M., Y.S., L.L., and A.M. designed the experiments. K.M. performed and analyzed cell-type-specific transsynaptic labeling experiments. Y.S. performed and analyzed in vivo electrophysiology. M.S. assisted 3D reconstruction and data analysis, and B.C.W. provided DNA constructs. K.M., Y.S., L.L., and A.M. wrote the manuscript, with contribution from B.C.W.

ACKNOWLEDGMENTS

We thank the Stanford Viral Core for help in generating AAVs, N. Uchida for reagents, C. Manalac for technical assistance, L. Cohen for assistance with electrophysiology, members of the Luo and Mizrahi Labs for discussion and critical reading of the manuscript, and T. Komiyama and J. Isaacson for communicating unpublished results. We thank D. Feldman and M. Feldman for financial support during the sabbatical of A.M. in the Luo Lab. K.M. is a Research Specialist and L.L. is an Investigator of the Howard Hughes Medical Institute. B.C.W. is an NSF Graduate Research Fellow and a Stanford Graduate Fellow. This work was also supported by a HHMI Collaborative Innovation Award, an NIH grant (R01-NS050835) to L.L., and a European Research Council Grant (number 203994) to A.M.

Accepted: August 20, 2013

Published: November 14, 2013

REFERENCES

- Aungst, J.L., Heyward, P.M., Puche, A.C., Karnup, S.V., Hayar, A., Szabo, G., and Shipley, M.T. (2003). Centre-surround inhibition among olfactory bulb glomeruli. *Nature* 426, 623–629.
- Batista-Brito, R., Close, J., Machold, R., and Fishell, G. (2008). The distinct temporal origins of olfactory bulb interneuron subtypes. *J. Neurosci.* 28, 3966–3975.
- Cleland, T.A. (2010). Early transformations in odor representation. *Trends Neurosci.* 33, 130–139.
- Cruikshank, S.J., Lewis, T.J., and Connors, B.W. (2007). Synaptic basis for intense thalamocortical activation of feedforward inhibitory cells in neocortex. *Nat. Neurosci.* 10, 462–468.
- Davison, I.G., and Katz, L.C. (2007). Sparse and selective odor coding by mitral/tufted neurons in the main olfactory bulb. *J. Neurosci.* 27, 2091–2101.
- Debarbieux, F., Audinat, E., and Charpak, S. (2003). Action potential propagation in dendrites of rat mitral cells in vivo. *J. Neurosci.* 23, 5553–5560.
- Denk, W., Briggman, K.L., and Helmstaedter, M. (2012). Structural neurobiology: missing link to a mechanistic understanding of neural computation. *Nat. Rev. Neurosci.* 13, 351–358.
- Dhawale, A.K., Hagiwara, A., Bhalla, U.S., Murthy, V.N., and Albeanu, D.F. (2010). Non-redundant odor coding by sister mitral cells revealed by light addressable glomeruli in the mouse. *Nat. Neurosci.* 13, 1404–1412.
- Egger, V., and Urban, N.N. (2006). Dynamic connectivity in the mitral cell-granule cell microcircuit. *Semin. Cell Dev. Biol.* 17, 424–432.
- Fantana, A.L., Soucy, E.R., and Meister, M. (2008). Rat olfactory bulb mitral cells receive sparse glomerular inputs. *Neuron* 59, 802–814.
- Gabernet, L., Jadhav, S.P., Feldman, D.E., Carandini, M., and Scanziani, M. (2005). Somatosensory integration controlled by dynamic thalamocortical feed-forward inhibition. *Neuron* 48, 315–327.
- Gibson, J.R., Beierlein, M., and Connors, B.W. (1999). Two networks of electrically coupled inhibitory neurons in neocortex. *Nature* 402, 75–79.
- Hamilton, K.A., Heinbockel, T., Ennis, M., Szabó, G., Erdélyi, F., and Hayar, A. (2005). Properties of external plexiform layer interneurons in mouse olfactory bulb slices. *Neuroscience* 133, 819–829.
- Hippenmeyer, S., Vrieseling, E., Sigrist, M., Portmann, T., Laengle, C., Ladle, D.R., and Arber, S. (2005). A developmental switch in the response of DRG neurons to ETS transcription factor signaling. *PLoS Biol.* 3, e159.
- Huang, L., Garcia, I., Jen, H.I., and Arenkiel, B.R. (2013). Reciprocal connectivity between mitral cells and external plexiform layer interneurons in the mouse olfactory bulb. *Front Neural Circuits* 7, 32.
- Igarashi, K.M., Ieki, N., An, M., Yamaguchi, Y., Nagayama, S., Kobayakawa, K., Kobayakawa, R., Tanifuji, M., Sakano, H., Chen, W.R., and Mori, K. (2012). Parallel mitral and tufted cell pathways route distinct odor information to different targets in the olfactory cortex. *J. Neurosci.* 32, 7970–7985.
- Inoue, T., and Imoto, K. (2006). Feedforward inhibitory connections from multiple thalamic cells to multiple regular-spiking cells in layer 4 of the somatosensory cortex. *J. Neurophysiol.* 96, 1746–1754.
- Iriki, A., Pavlides, C., Keller, A., and Asanuma, H. (1989). Long-term potentiation in the motor cortex. *Science* 245, 1385–1387.
- Isaacson, J.S., and Scanziani, M. (2011). How inhibition shapes cortical activity. *Neuron* 72, 231–243.
- Jahr, C.E., and Nicoll, R.A. (1980). Dendrodendritic inhibition: demonstration with intracellular recording. *Science* 207, 1473–1475.
- Kato, H.K., Chu, M.W., Isaacson, J.S., and Komiyama, T. (2012). Dynamic sensory representations in the olfactory bulb: modulation by wakefulness and experience. *Neuron* 76, 962–975.
- Kato, H.K., Gillet, S.N., Peters, A.J., Isaacson, J.S., and Komiyama, T. (2013). Parvalbumin-expressing interneurons linearly control olfactory bulb output.

- Neuron 80. Published online November 14, 2013. <http://dx.doi.org/10.1016/j.neuron.2013.08.036>.
- Kikuta, S., Fletcher, M.L., Homma, R., Yamasoba, T., and Nagayama, S. (2013). Odorant response properties of individual neurons in an olfactory glomerular module. *Neuron* 77, 1122–1135.
- Kosaka, T., and Kosaka, K. (2008). Heterogeneity of parvalbumin-containing neurons in the mouse main olfactory bulb, with special reference to short-axon cells and betaIV-spectrin positive dendritic segments. *Neurosci. Res.* 60, 56–72.
- Kosaka, T., and Kosaka, K. (2011). “Interneurons” in the olfactory bulb revisited. *Neurosci. Res.* 69, 93–99.
- Kosaka, K., Heizmann, C.W., and Kosaka, T. (1994). Calcium-binding protein parvalbumin-immunoreactive neurons in the rat olfactory bulb. 1. Distribution and structural features in adult rat. *Exp. Brain Res.* 99, 191–204.
- Kozak, M. (1987). An analysis of 5′-noncoding sequences from 699 vertebrate messenger RNAs. *Nucleic Acids Res.* 15, 8125–8148.
- Kuhlman, S.J., Tring, E., and Trachtenberg, J.T. (2011). Fast-spiking interneurons have an initial orientation bias that is lost with vision. *Nat. Neurosci.* 14, 1121–1123.
- Luo, L., Callaway, E.M., and Svoboda, K. (2008). Genetic dissection of neural circuits. *Neuron* 57, 634–660.
- Madisen, L., Zwingman, T.A., Sunkin, S.M., Oh, S.W., Zariwala, H.A., Gu, H., Ng, L.L., Palmiter, R.D., Hawrylycz, M.J., Jones, A.R., et al. (2010). A robust and high-throughput Cre reporting and characterization system for the whole mouse brain. *Nat. Neurosci.* 13, 133–140.
- Margrie, T.W., Sakmann, B., and Urban, N.N. (2001). Action potential propagation in mitral cell lateral dendrites is decremental and controls recurrent and lateral inhibition in the mammalian olfactory bulb. *Proc. Natl. Acad. Sci. USA* 98, 319–324.
- Margrie, T.W., Meyer, A.H., Caputi, A., Monyer, H., Hasan, M.T., Schaefer, A.T., Denk, W., and Brecht, M. (2003). Targeted whole-cell recordings in the mammalian brain in vivo. *Neuron* 39, 911–918.
- Marshall, J.H., Mori, T., Nielsen, K.J., and Callaway, E.M. (2010). Targeting single neuronal networks for gene expression and cell labeling in vivo. *Neuron* 67, 562–574.
- Miyamichi, K., Amat, F., Moussavi, F., Wang, C., Wickersham, I., Wall, N.R., Taniguchi, H., Tasic, B., Huang, Z.J., He, Z., et al. (2011). Cortical representations of olfactory input by trans-synaptic tracing. *Nature* 472, 191–196.
- Monyer, H., and Markram, H. (2004). Interneuron Diversity series: Molecular and genetic tools to study GABAergic interneuron diversity and function. *Trends Neurosci.* 27, 90–97.
- Mori, K., Nagao, H., and Yoshihara, Y. (1999). The olfactory bulb: coding and processing of odor molecule information. *Science* 286, 711–715.
- Murthy, V.N. (2011). Olfactory maps in the brain. *Annu. Rev. Neurosci.* 34, 233–258.
- Nagai, Y., Sano, H., and Yokoi, M. (2005). Transgenic expression of Cre recombinase in mitral/tufted cells of the olfactory bulb. *Genesis* 43, 12–16.
- Nagayama, S., Takahashi, Y.K., Yoshihara, Y., and Mori, K. (2004). Mitral and tufted cells differ in the decoding manner of odor maps in the rat olfactory bulb. *J. Neurophysiol.* 91, 2532–2540.
- Olsen, S.R., Bhandawat, V., and Wilson, R.I. (2010). Divisive normalization in olfactory population codes. *Neuron* 66, 287–299.
- Poo, C., and Isaacson, J.S. (2009). Odor representations in olfactory cortex: “sparse” coding, global inhibition, and oscillations. *Neuron* 62, 850–861.
- Rong, L., Gendron, K., Strohl, B., Shenoy, R., Wool-Lewis, R.J., and Bates, P. (1998). Characterization of determinants for envelope binding and infection in tva, the subgroup A avian sarcoma and leukosis virus receptor. *J. Virol.* 72, 4552–4559.
- Sakano, H. (2010). Neural map formation in the mouse olfactory system. *Neuron* 67, 530–542.
- Schoenfeld, T.A., Marchand, J.E., and Macrides, F. (1985). Topographic organization of tufted cell axonal projections in the hamster main olfactory bulb: an intrabulbar associational system. *J. Comp. Neurol.* 235, 503–518.
- Shepherd, G.M. (2004). *The Synaptic Organization of the Brain*, Fifth Edition. (Oxford: Oxford University Press).
- Shepherd, G.M., Chen, W.R., Willhite, D., Migliore, M., and Greer, C.A. (2007). The olfactory granule cell: from classical enigma to central role in olfactory processing. *Brain Res. Brain Res. Rev.* 55, 373–382.
- Sohal, V.S., Zhang, F., Yizhar, O., and Deisseroth, K. (2009). Parvalbumin neurons and gamma rhythms enhance cortical circuit performance. *Nature* 459, 698–702.
- Sohya, K., Kameyama, K., Yanagawa, Y., Obata, K., and Tsumoto, T. (2007). GABAergic neurons are less selective to stimulus orientation than excitatory neurons in layer II/III of visual cortex, as revealed by in vivo functional Ca2+ imaging in transgenic mice. *J. Neurosci.* 27, 2145–2149.
- Song, J., Zhong, C., Bonaguidi, M.A., Sun, G.J., Hsu, D., Gu, Y., Meletis, K., Huang, Z.J., Ge, S., Enikolopov, G., et al. (2012). Neuronal circuitry mechanism regulating adult quiescent neural stem-cell fate decision. *Nature* 489, 150–154.
- Tan, J., Savigner, A., Ma, M., and Luo, M. (2010). Odor information processing by the olfactory bulb analyzed in gene-targeted mice. *Neuron* 65, 912–926.
- Taniguchi, H., He, M., Wu, P., Kim, S., Paik, R., Sugino, K., Kvitsiani, D., Fu, Y., Lu, J., Lin, Y., et al. (2011). A resource of Cre driver lines for genetic targeting of GABAergic neurons in cerebral cortex. *Neuron* 71, 995–1013.
- Tiesinga, P., and Sejnowski, T.J. (2009). Cortical enlightenment: are attentional gamma oscillations driven by ING or PING? *Neuron* 63, 727–732.
- Wall, N.R., Wickersham, I.R., Cetin, A., De La Parra, M., and Callaway, E.M. (2010). Monosynaptic circuit tracing in vivo through Cre-dependent targeting and complementation of modified rabies virus. *Proc. Natl. Acad. Sci. USA* 107, 21848–21853.
- Watabe-Uchida, M., Zhu, L., Ogawa, S.K., Vamanrao, A., and Uchida, N. (2012). Whole-brain mapping of direct inputs to midbrain dopamine neurons. *Neuron* 74, 858–873.
- Whitesell, J.D., Sorensen, K.A., Jarvie, B.C., Hentges, S.T., and Schoppa, N.E. (2013). Interglomerular lateral inhibition targeted on external tufted cells in the olfactory bulb. *J. Neurosci.* 33, 1552–1563.
- Wickersham, I.R., Lyon, D.C., Barnard, R.J., Mori, T., Finke, S., Conzelmann, K.K., Young, J.A., and Callaway, E.M. (2007). Monosynaptic restriction of transsynaptic tracing from single, genetically targeted neurons. *Neuron* 53, 639–647.
- Willhite, D.C., Nguyen, K.T., Masurkar, A.V., Greer, C.A., Shepherd, G.M., and Chen, W.R. (2006). Viral tracing identifies distributed columnar organization in the olfactory bulb. *Proc. Natl. Acad. Sci. USA* 103, 12592–12597.
- Yokoi, M., Mori, K., and Nakanishi, S. (1995). Refinement of odor molecule tuning by dendrodendritic synaptic inhibition in the olfactory bulb. *Proc. Natl. Acad. Sci. USA* 92, 3371–3375.

Neuron, Volume 80

Supplemental Information

Dissecting Local Circuits:

Parvalbumin Interneurons Underlie Broad

Feedback Control of Olfactory Bulb Output

**Kazunari Miyamichi, Yael Shlomei-Fuchs, Marvin Shu, Brandon C. Weissbourd, Liqun Luo,
and Adi Mizrahi**

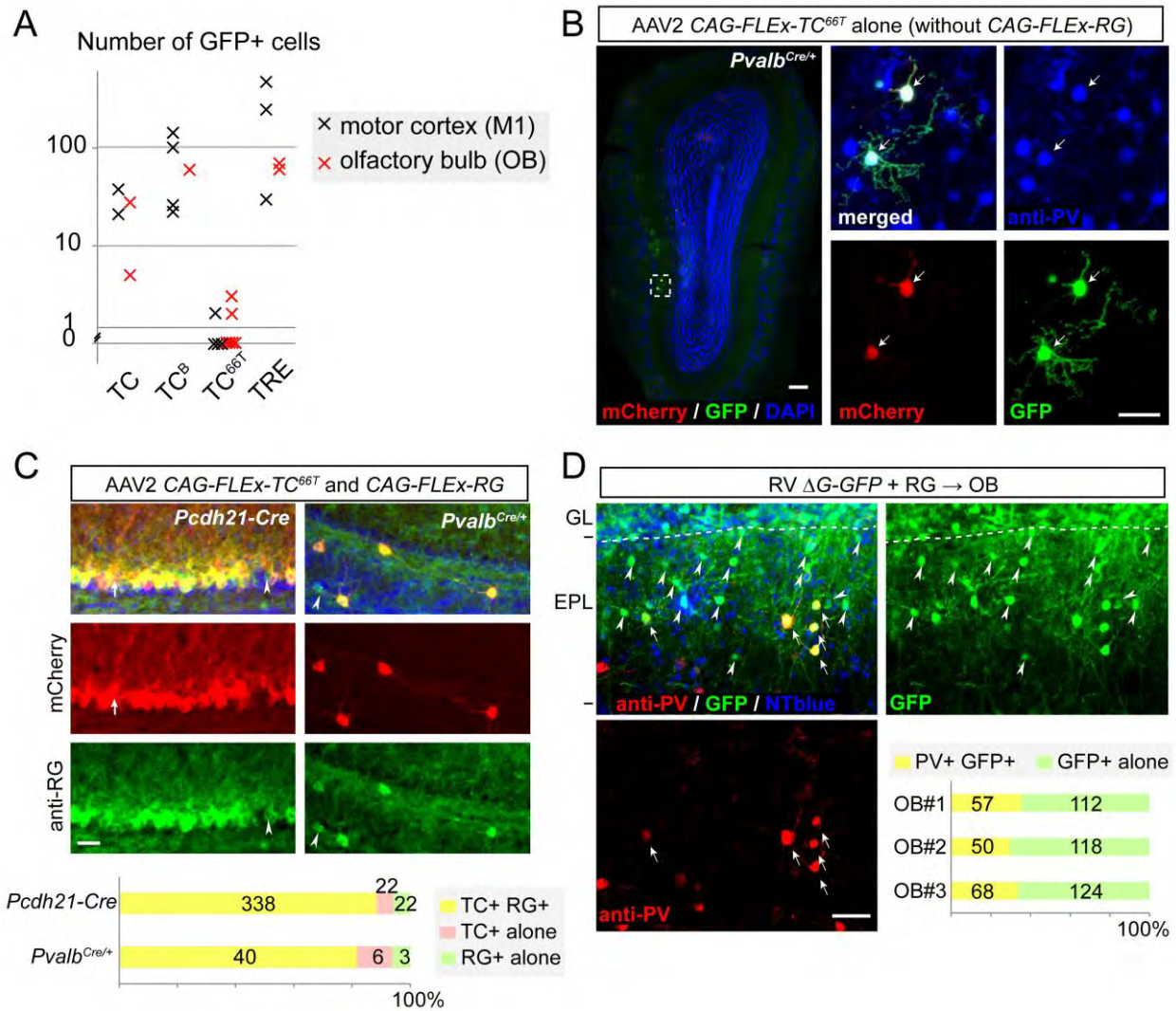


Figure S1. Additional Control Experiments for Cell Type-Specific Transsynaptic Labeling, Related to Figure 1.

(A) Estimating non-specific labeling by RV due to leaky TVA expression. Quantification of GFP+ cells in experiments with wild-type mice using AAV2 *EF1a-FLEX-TC* (Watabe-Uchida et al., 2012), *CAG-FLEX-TC^B*, *CAG-FLEX-TC^{66T}* and *TRE-HTG* (Miyamichi et al., 2011). Because the TVA receptor is highly sensitive to EnvA-pseudotyped rabies virus (Seidler et al., 2008; Wall et al., 2010), a small amount of leaky expression of TVA from Cre-dependent viruses in the absence of Cre (Wall et al., 2010; Watabe-Uchida et al., 2012), or tTA2-dependent viruses in the absence of tTA2 (Miyamichi et al., 2011), can cause non-specific initial infection of the RV. The density of this non-specific labeling can vary by brain regions and by the titer of AAV and RV. Indeed, when we used higher titer RV and AAV in the tTA2/TRE-based strategy, we found >10-fold non-specific labeling of RV in the local injection site than we previously reported (Miyamichi et al., 2011). Therefore, we compared side-by-side four different strategies in the neocortex of wild-type mice to assess the Cre or tTA2 independent non-specific rabies labeling. The numbers of RV labeled cells in wild-type animals are plotted, with each cross (black, motor cortex; red, olfactory bulb) representing

one independent experiment. Only TC^{66T} -based strategy has nearly 0 non-specific labeling.

(B) Testing RG-dependency of transsynaptic RV spread. AAV2 *CAG-FLEX-TC^{66T}* alone (without *CAG-FLEX-RG*) was injected into the olfactory bulb (OB) of *Pvalb^{Cre/+}* mouse (Hippenmeyer et al., 2005). Two week later, RV $\Delta G-GFP+EnvA$ was injected into the same area. A single 60- μm coronal section stained with anti-PV antibodies is shown. 20 ± 2.6 GFP+ neurons (n=3 animals) were found near the injection site, and all of them were labeled with mCherry and anti-PV (indicated by arrows), demonstrating that our AAV *FLEX* vector is specifically activated in the Cre-positive neurons *in vivo*. Importantly, in the absence of AAV *CAG-FLEX-RG*, RV transduction was almost completely limited to the mCherry+ populations. Non-specific GFP expression outside the mCherry+ population was 2 ± 0.6 cells per animal (n=3), which is within the range of Cre-independent labeling in the wild-type control (panel A, TC^{66T}). These data confirmed that transsynaptic spread of RV strictly depends on the function of RG. Scale bars, 100 μm for the left panel; 25 μm for the right four panels.

(C) Testing co-transduction efficiency of AAV2 *CAG-FLEX-RG* and AAV2 *CAG-FLEX-TC^{66T}*. Because RG and TC (TVA-mCherry) are driven by two independent AAVs (Watabe-Uchida et al., 2012), some neurons may receive only one of these two AAV vectors. RG-/TC+ neurons can receive EnvA pseudotyped RV and therefore are indistinguishable from the starter cells, but cannot produce infectious RV due to the lack of RG (we term these pseudo-starter cells). RG+/TC- neurons can trans-synaptically receive RV if they are the presynaptic partners of one of the starter cells, and can generate infectious RV, even though they are not labeled with mCherry (we term these invisible starter cells). To test the abundance and distribution of pseudo-starter cells and invisible starter cells, we injected into *Pcdh21-Cre* (n=3) and *Pvalb^{Cre/+}* (n=3) a 1:1 mixture of *CAG-FLEX-RG* and *CAG-FLEX-TC^{66T}* and stained sections with anti-RG antibodies. Within 400 μm around the injection site, 88.6% (*Pcdh21-Cre*) and 81% (*Pvalb^{Cre/+}*) of labeled neurons were dually labeled with TC and RG. As starter cells tend to cluster near the injection site, these data indicate that most of our TC+ cells are bona fide starter cells. RG+/TC- (indicated by arrowheads) or RG-/TC+ (indicated by arrows) were a minority near the injection site, although RG-/TC+ neurons were sometimes more broadly distributed than RG+/TC- neurons. Thus, pseudo-starter cells may be present in the periphery of the injection site, and this could lead to an over-estimate of the spatial spread of the starter cells in our experiments. Scale bar, 25 μm .

(D) To test if non-PV neurons in the EPL (Huang et al., 2013; Lepousez et al., 2010) are competent to receive RV, we made use of the *in vitro* complemented RV $\Delta G-GFP+RG$. This virus can infect cells that would be infected by the wild-type RV but cannot produce further viral particles for transsynaptic transmission (Miyamichi et al., 2011; Wickersham et al., 2007). 0.3 μl of RV $\Delta G-GFP+RG$ was injected into the lateral surface of the OB (n=3), and EPL neurons were analyzed 4 days later. A typical example of a 60- μm coronal section near the injection site is shown. In total, $33 \pm 1.6\%$ GFP+ neurons in the EPL were co-stained with anti-PV antibodies (arrows), while many non-PVNs were labeled with GFP (arrowheads). This is markedly different from transduction of cells

trans-synaptically from M/T cells (Figure 2B), where $88 \pm 1.6\%$ GFP+ neurons were PVNs ($p < 0.001$, t-test). Thus, transsynaptic RV spread specifically labeled a sub-population of all RV competent neurons in EPL, supporting synaptic specificity of RV spread in vivo. Scale bar, 25 μm .

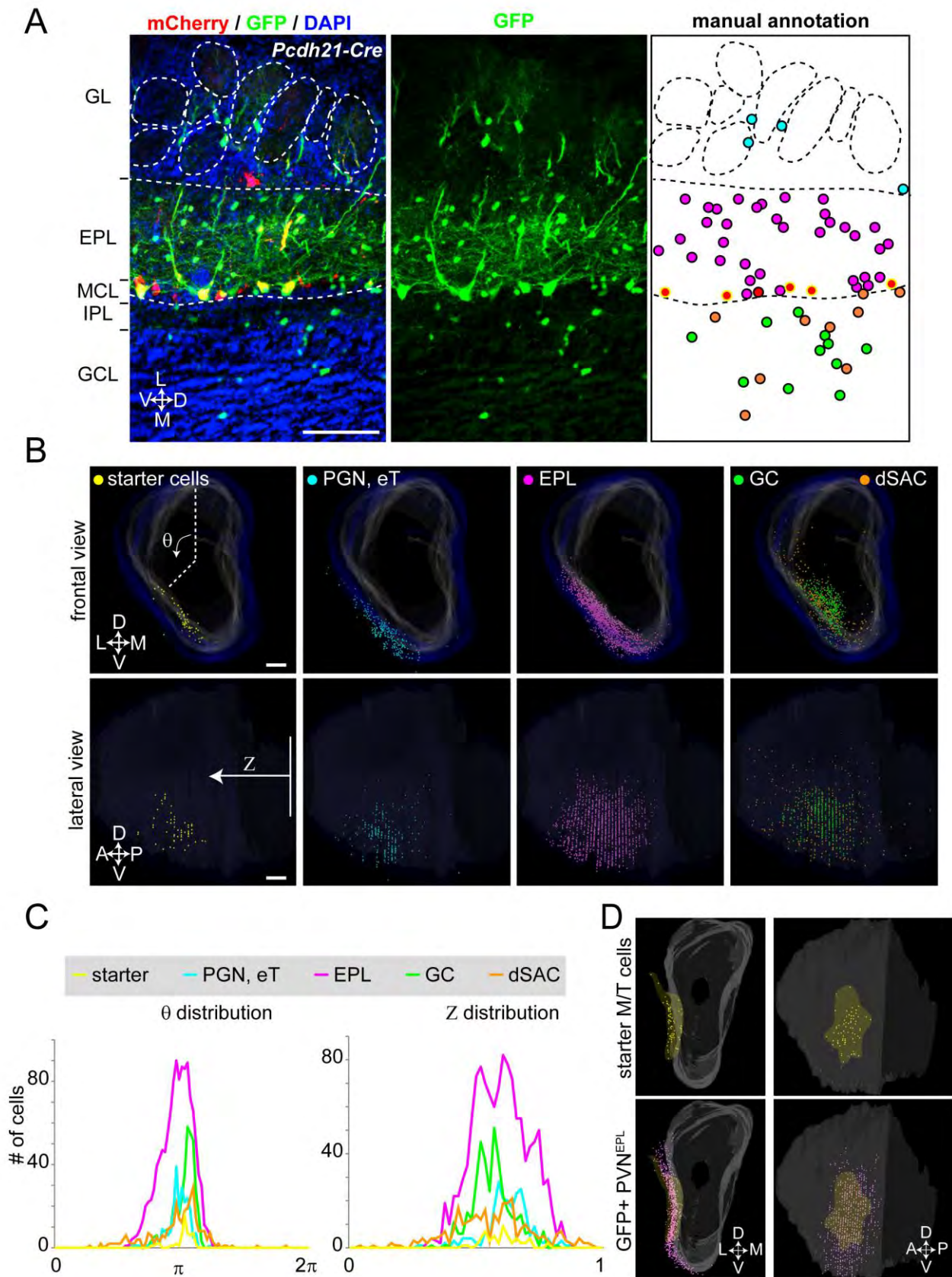


Figure S2. 3D Reconstruction of the Labeled OB Samples, Related to Figure 2.

(A) A typical 60- μm OB section with five starter MCs and many GFP+ neurons. After detecting the

mitral cell layer and the boundary between the glomerular layer and EPL, we manually annotated starter cells (with a yellow contour) and GFP-labeled presynaptic neurons in different layer and/or of different cell types with differently colored circles (GL, cyan; EPL, magenta; MC, red; GC, green; and dSAC, orange). A custom-made MATLAB program automatically assembles these manual annotations to form 3D reconstructions (see Supplemental Experimental Procedures for details). Scale bar, 100 μm .

(B) Frontal (top panels) and lateral (bottom panels) views of a 3D reconstructed OB model from a *Pcdh21-Cre* tracing experiment. White shadow represents the mitral cell layer, and the blue shadow represents the boundary between the GL and EPL. In this sample, 51 starter MCs and 3 starter external tufted cells (eTs) were found in the ventro-lateral area of the OB (yellow dots). 465 GFP+ neurons in GL are shown in cyan dots, which contain periglomerular cells (PGNs) and eTs. 1225 GFP+ cells in the EPL (magenta), 380 GCs (granule cells, green) and 302 dSACs (deep short axon cells, orange) are also shown side by side. As shown in Figure 2C and 2D, the labeled dots were quantified in the cylindrical coordinate system (θ for the rotation angle from the dorsal polar axis, Z for the distance from the most posterior section). Scale bar, 100 μm .

(C) Histograms showing the distribution of θ and Z for each group (colors of the line in the histogram match the colors of the dots in panel A and B).

(D) Another 3D-reconstructed OB model from a different *Pcdh21-Cre* tracing sample, where 53 external tufted cells and 14 MCs were identified as starter cells (shown in yellow). As in Figure 2C, we stained every section from this sample with anti-PV antibody and identified 752 (out of 855 GFP+ EPL cells, 88%) were PVNs^{EPL} (shown in magenta). Areas of starter cells are highlighted by yellow shadows.

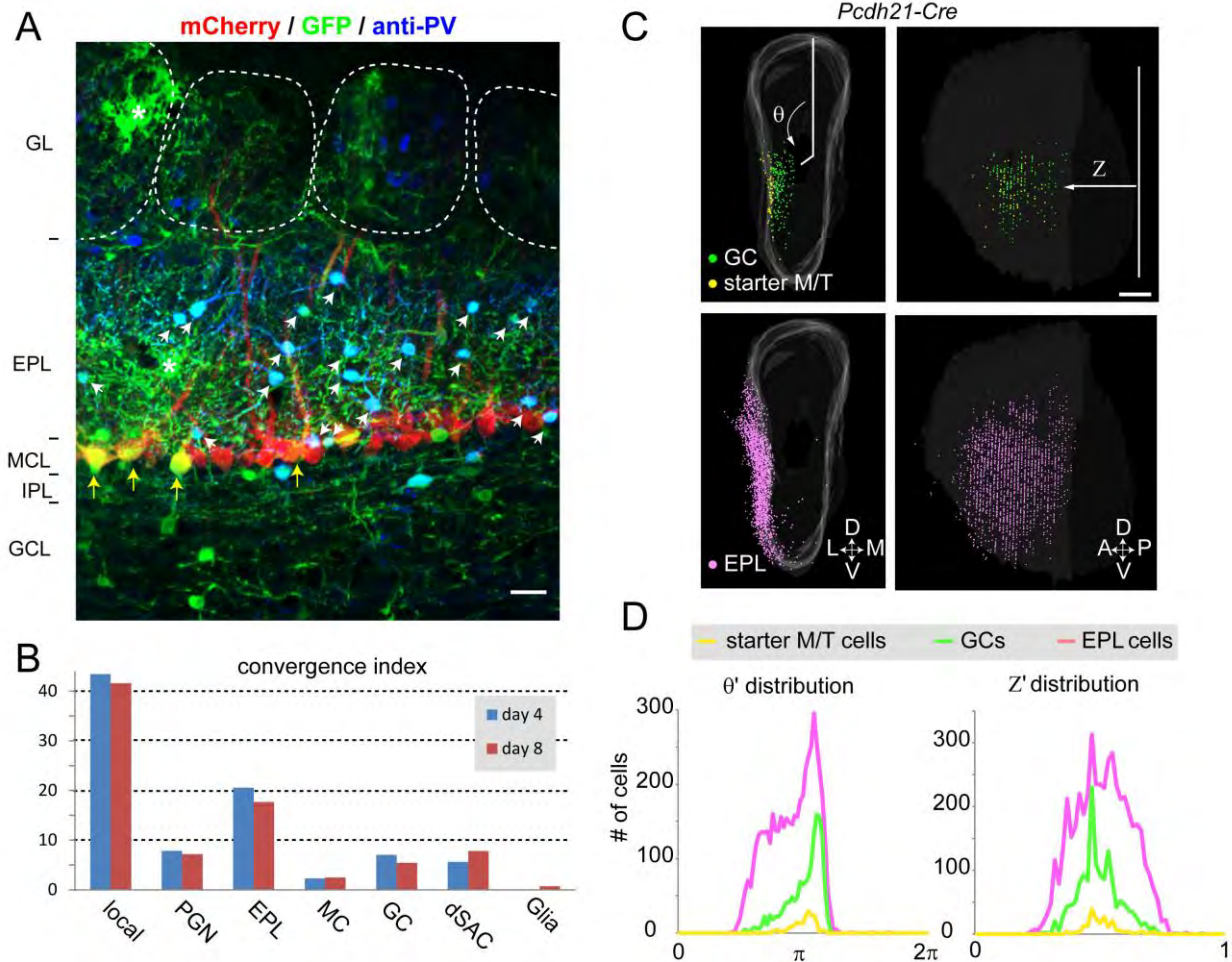


Figure S3. Longer Survival Period After RV Infection Does Not Change Labeling Patterns, Related to Figure 2.

(A) To test if a longer survival period alters the pattern of transsynaptic spread of RV, we used the *CAG-FLEX-TC^{66T}*-based transsynaptic tracing strategy in *Pcdh21-Cre* mice (as in Figure 2) and waited for 8 days after RV injection instead of the 4 days used for data described for all other experiments. We obtained two samples, with a total of 272 starter M/Ts and 11,317 local GFP+ cells across all layers of the OB. Shown here is a typical 60- μ m coronal OB section stained by anti-PV antibodies containing starter MCs (yellow arrows) and GFP+ presynaptic neurons. GL, glomerular layer; EPL, external plexiform layer; MCL, mitral cell layer; IPL, internal plexiform layer; GCL, granule cell layer. Neurons co-labeled with GFP and anti-PV antibodies in the EPL are indicated by white arrows. Glial processes are indicated by asterisks. Scale bar, 20 μ m.

(B) The convergence indices (the number of GFP+ cells divided by the number of starter cells) for the pooled day 4 and day 8 samples. Length of survival period did not change the convergence indices or layer distributions of GFP+ cells. Notably, we detected a significant number of glia cells only in day 8 samples.

(C) Frontal (left panels) and lateral (right panels) views of a 3D reconstructed OB model of a day 8

sample. In this sample, we found 50 starter MCs (yellow, top panels), 169 putative pre-synaptic GCs (green, top panels), and 1,809 putative pre-synaptic neurons in the EPL (magenta, bottom panels). As we observed in Figure 7C and Figure S2, GFP+ GCs clusters are close to starter MCs. In contrast, GFP+ cells in the EPL were more broadly distributed than starter MCs, as we observed in day 4 samples (Figure S2B, C).

(D) Histograms showing the distribution of normalized and pooled θ' and Z' values for each group in the 8-day experiment (the colors of the lines in the histogram match the colors of the dots in panel C).

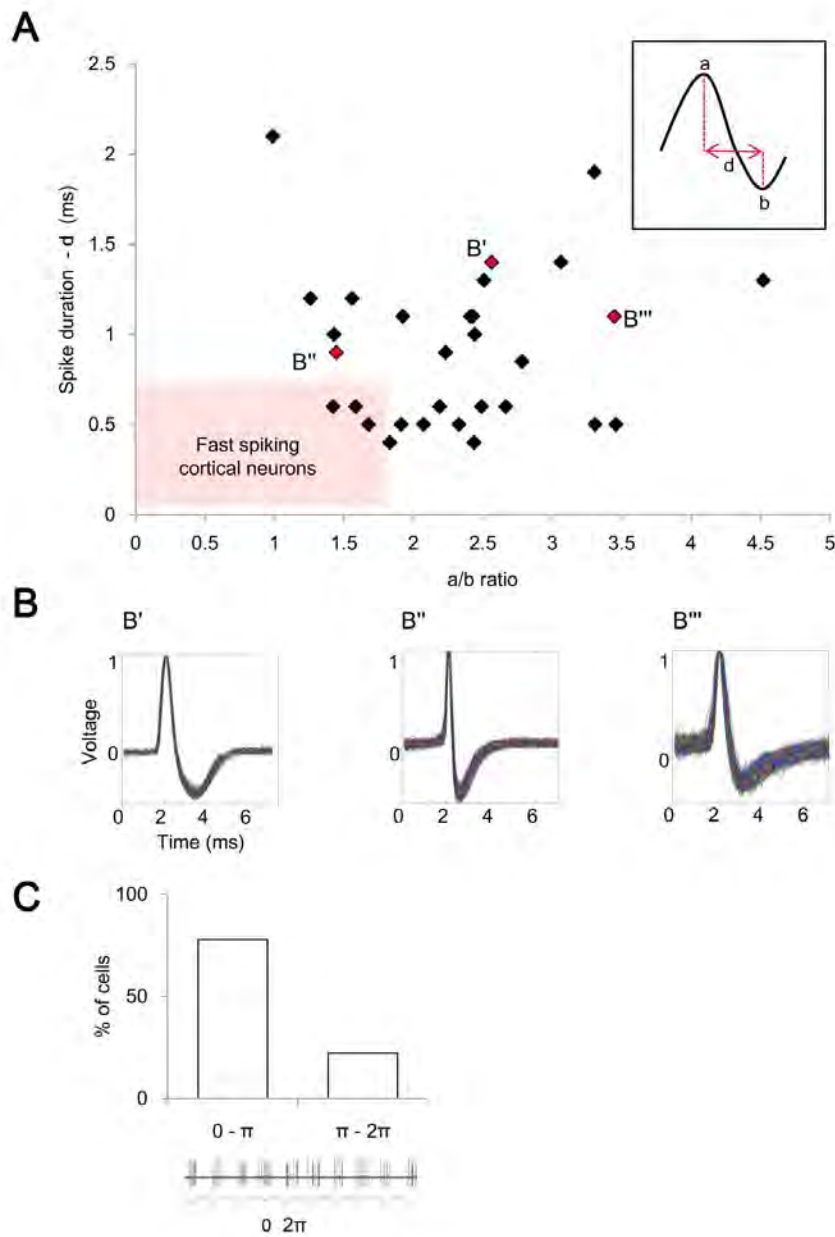


Figure S4. Spontaneous Electrophysiological Properties of PVN^{EPL}, Related to Figure 3.

(A) The spike waveforms of all PVN^{EPL} in our data set were characterized by spike peak (a, inset) to valley (b, inset) ratio relative to spike peak to valley duration (d, inset). Red area indicates the threshold for waveform characteristics of cortical fast spiking neurons.

(B) Examples of the spike waveform of 3 different PVN^{EPL} denoted B'-B''' in A. Colored lines represent individual spike waveforms, dashed black line represents mean waveform.

(C) Spontaneous phase tuning of PVN^{EPL}. Top, histogram of the spontaneous phase tuning of PVN^{EPL}. Bottom, raw spiking traces of spontaneous activity shown with regard to the respiration. Red lines mark the start (0) and end (2π) of one respiration cycle.

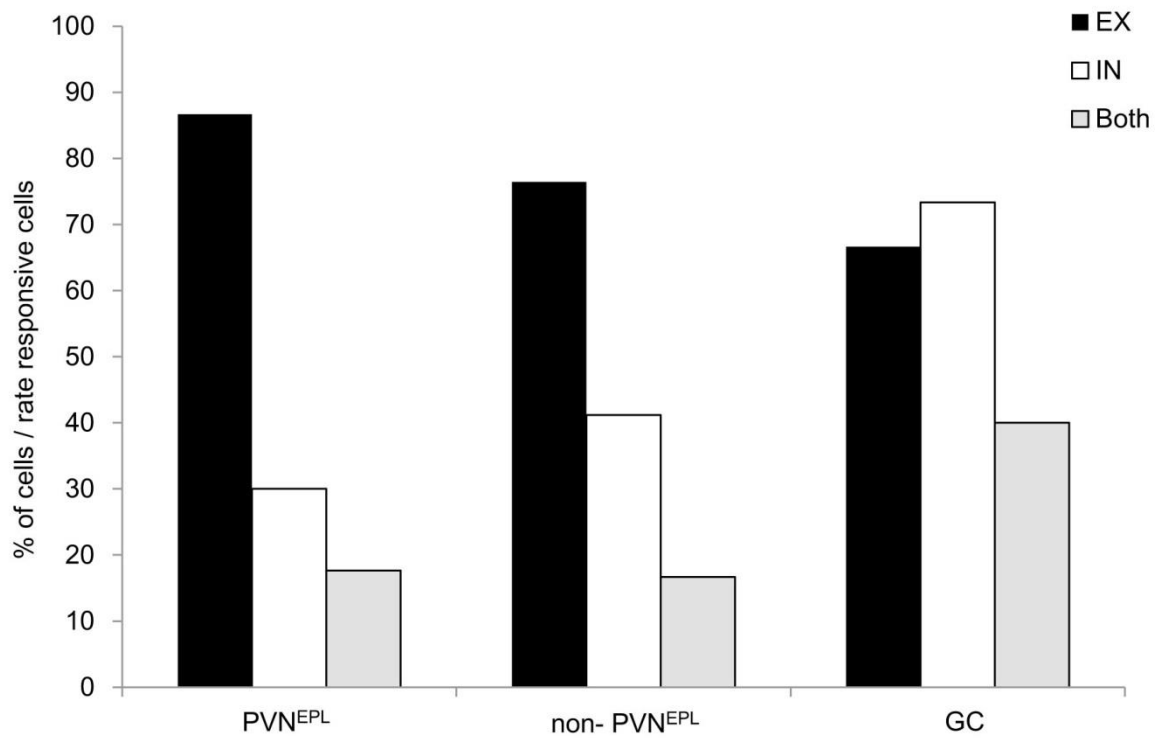


Figure S5. Most PVNs Show Exclusively Excitatory or Exclusively Inhibitory Odor-Evoked Responses, Related to Figure 5.

Histogram of the percentage of cells responding with inhibition, excitation or both, for all cell groups. Only cells that showed changes in spike rates are included.

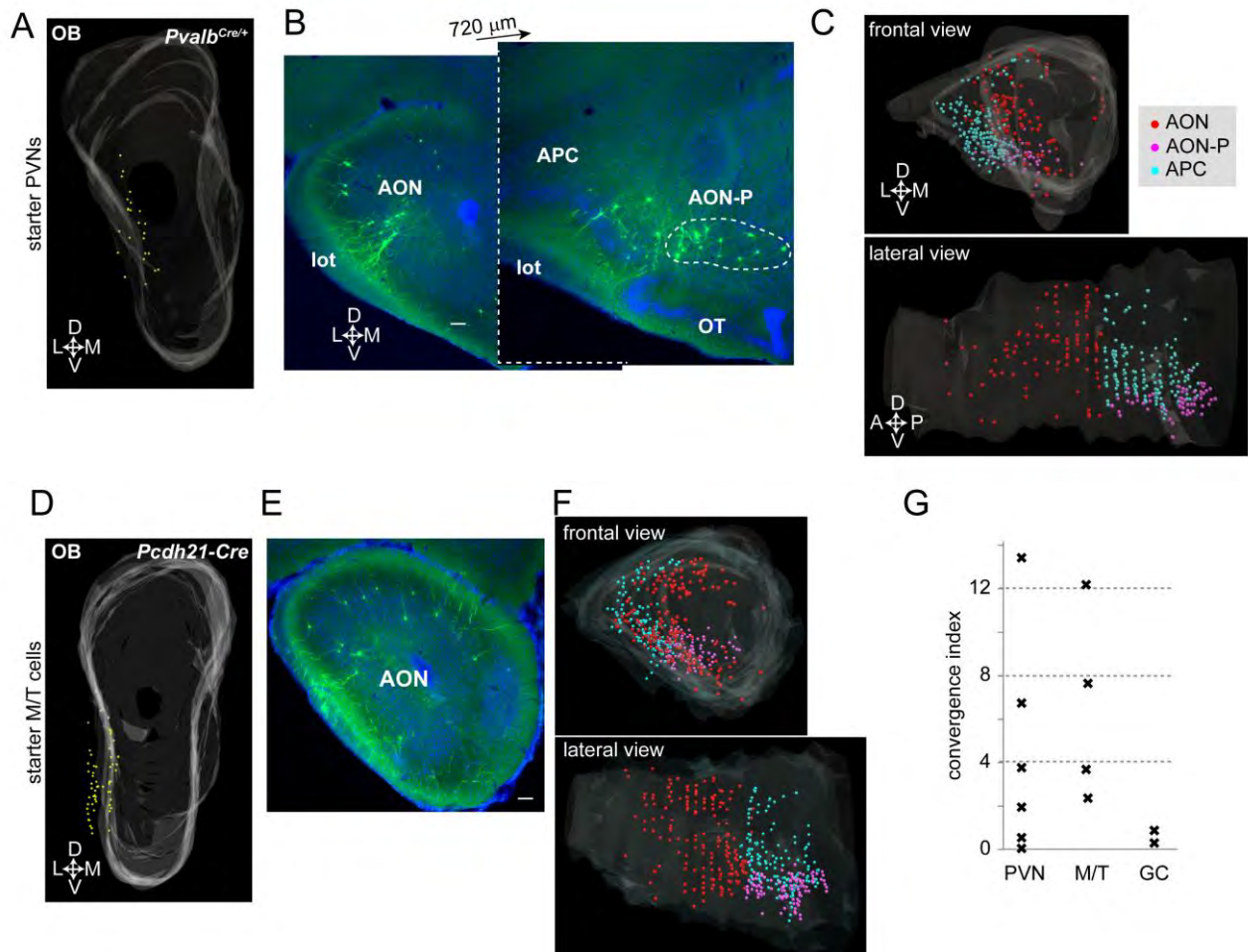


Figure S6. Cortical Feedback Projections to PVNs and Mitral/Tufted Cells in the OB, Related to Figure 2 and Figure 6.

(A) A 3D-reconstructed *Pvalb^{Cre/+}* OB sample showing starter PVNs (21 PVNs^{IPL} and 3 PVNs^{EPL}) in the ventro-lateral part of the OB. In this sample, 101 GFP+ neurons were found in the anterior olfactory nucleus lateral, dorsal, and ventral division (hereafter referred to as AON for simplicity), 61 GFP+ neurons were found in AON posterior division (AON-P) (Brunjes et al., 2005), and 164 GFP+ neurons were identified in the anterior piriform cortex (APC). These observations indicate that PVNs in the OB directly receive cortical feedback projections.

(B) Typical examples of single 60-µm sections containing GFP+ AON and APC cortical neurons. OT, olfactory tubercle; lot, lateral olfactory tract. Scale bar, 100 µm.

(C) To visualize the spatial distribution of GFP+ neurons in the AON/APC, we used a previously established custom-made 3D-reconstruction program (Miyamichi et al., 2011). GFP+ neurons are shown as colored dots according to the location of their cell bodies, in the frontal (top) and lateral (bottom) views. White surface represents the boundary between layer I and layer II of the AON and APC. The GFP+ neurons were distributed broadly throughout the AON and anterior APC, suggesting a lack of apparent topographic organization of cortical feedback projections to the PVNs in the OB.

Data presented in panel (A-C) are originated from the same animal.

(D) A 3D reconstructed *Pcdh21-Cre* OB sample showing starter M/T cells (the same as Figure 2C) in the ventro-lateral part of the OB. In this sample, 181 AON neurons, 100 AON-P neurons, and 166 APC neurons were GFP+, suggesting direct cortical feedback input to the M/T cells.

(E) A representative example of a single 60- μ m section containing GFP+ AON cortical neurons. Scale bar, 100 μ m.

(F) Spatial distribution of GFP+ neurons in AON/APC, as in the panel (C). Data presented in panel (D-F) originated from the same animal.

(G) Convergence index (defined by the number of GFP+ cortical neurons divided by the number of starter OB neurons) is plotted for the three different starter cell populations in the OB: PVN by *Pvalb^{Cre/+}* (Figure 6), M/T cells by *Pcdh21-Cre* (Figure 2), and GC by *GAD2^{Cre/+}* (Figure 7).

Supplemental Experimental Procedures

Constructs and Virus Preparations

CAG-FLEX-RG, *CAG-FLEX-TC^B*, and *CAG-FLEX-TC^{66T}* cassette were constructed using standard molecular cloning methods with enzymes commercially available from New England Biolabs (Ipswich, USA). Specifically, the 330-base pair synthesized DNA fragment shown below was obtained from DNA 2.0 (Menlo Park, USA). This DNA fragment contained restriction enzyme sites and two heterospecific pairs of loxP (shown by underline) and *lox2272* (shown by italic) in the following order:

NotI-MluI-XmaI-*lox2272(c)*-loxP(c)-Sall-AscI-*lox2272*-loxP-HindIII-SpeI-NotI.

5'-GCGGCCGCACGCGTAATCCC GGGATAACTTCGTATAAAGTATCCTATACGAAGTTATATCA
AAATAGGAAGACCAATGCTTCACCATCGACCCGAATTGCCAAGCATCACCATCGACACAT
AACTTCGTATAATGTATGCTATACGAAGTTATGTCGACATATGGCGCGCCTATAACTTCGTAT
AGGATACTTTATACGAAGTTATCATTGGGATTCTTCCTATTTTGATCCAAGCATCACCATCGAC
CCTCTAGTCCAGATCTCACCATCGACCCATAACTTCGTATAGCATAACATTATACGAAGTTAT
AAGCTTAATTACTAGTGCGGCCGC-3'

After cloning this DNA fragment into the modified *pBluescript* vector that only contains a NotI site in the cloning site, the following DNA fragments were sub-cloned by using the unique restriction sites.

- 1) A DNA fragment containing the *WPRES* sequence and transcription termination signal from human growth hormone gene (*hGHpA*) was obtained from *pAAV-TRE-HTG* plasmid (Miyamichi et al., 2011) by using HindIII and SpeI restriction enzymes.
- 2) A DNA fragment containing the *CAG* promoter flanked by PstI (blunt ended by Klenow fragment) and XmaI sites was obtained from plasmid *pCA-G-intron-T* (Tasic et al., 2012). MluI (blunt ended by Klenow fragment) and XmaI sites in our vector were used for sub-cloning.
- 3-1) A PCR fragment was amplified using Phusion Taq polymerase from *pAAV-CAG-FLEX-RG* and *pAAV-EF1a-FLEX-TVA-mCherry* (Watabe-Uchida et al., 2012). The following primers including a Kozak sequence (underlined) before the initiation codon (italic) were used:

For the *RG* cassette,

5'-GGCGCGCCACCATGGTTCCTCAGGCTCTCCT:

5'-GTCGACTTACAGTCTGGTCTCACCCC

For *TC^B* cassette,

5'-GGCGCGCCACCATGGCGCGGCTGCTGCCCGC:

5'-GTCGACTTACTTGTACAGCTCGTCCA

These cassettes were flanked by AscI and Sall.

- 3-2) The *TC^{66T}* cassette was produced using PCR based introduction of the point mutation into the TVA receptor. Note that the point mutation in our vector (E66^T) corresponds to the E47^T mutation in the TVA800 (Rong et al., 1998). A part of TVA receptor gene was amplified with

the point mutation (GAG→ACC) by Phusion Taq polymerase using the plasmid *pAAV-EF1a-FLEX-TVA-mCherry* (Watabe-Uchida et al., 2012) as a template. This PCR product (208 base pairs) also contains the restriction site *AscI*, and the kozak sequence (underlined) located immediately upstream of the initiation codon (italic). The following PCR primers were used.:

5'-GGCGCGCCACCATGGCGCGGCTGCTGCCCCGC:

5'-GGTGTCCCGCCCGTCGTCGAGT

The rest of the sequence for the TVA receptor fused with mCherry was amplified from the same template *pAAV-EF1a-FLEX-TVA-mCherry* using the following PCR primers:

5'-GCGACGACGGGCGGGACACCTGGGGCTGCGGGACCAGCGC:

5'-GTCGACTTACTTGTACAGCTCGTCCA.

These two PCR products were then mixed together and used as a template to obtain the full length TC^{66T} cassette flanked by *AscI* and *Sall* restriction sites by using the PCR primers:

5'-GGCGCGCCACCATGGCGCGGCTGCTGCCCCGC.

5'-GTCGACTTACTTGTACAGCTCGTCCA.

The assembled cassettes were sub-cloned into *pAAV-MCS* (AAV helper free system, Stratagene, Cat#240071-12) using the *NotI* site. The final constructs *CAG-FLEX-TC^B*, and *CAG-FLEX-TC^{66T}* were tested by transient transfection into cultured HEK293 cells, using *EF1a-FLEX-TC* as a reference (Figure 1). Using 6-well plates, 1.5µg of the each circular plasmid, with or without 1.5µg of a Cre-encoding plasmid *pBT140* (*CMV* promoter driving nuclear localization signal-*Cre*), was introduced into the HEK293 cells using Lipofectamine 2000 (Invitrogen, Cat#11668-027) according to the manufacture's instructions. Fluorescence of mCherry was detected 72 hours post-transfection.

All viral procedures followed the Biosafety Guidelines approved by the Stanford University Administrative Panel on Laboratory Animal Care (A-PLAC) and Administrative Panel of Biosafety (APB). Recombinant AAV vectors (serotype 2) were produced in the Stanford Viral Core. The AAV titer was estimated to be 1.6, 5.6, and 2.8 x 10¹¹ viral particles/ml for *CAG-FLEX-RG*, *CAG-FLEX-TC^B*, and *CAG-FLEX-TC^{66T}*, respectively, based on quantitative PCR analysis. Pseudotyped ΔG RV was prepared as previously described (Wickersham et al., 2007; Wickersham et al., 2010). The pseudotyped RV titer was estimated to be ~5 x 10⁹ infectious particles/ml based on serial dilutions of the virus stock followed by infection of the 293-TVA800 cell line.

Two-Photon Targeted Recording from PV-Positive Neurons

Imaging of the OB was performed using an Ultima two-photon microscope from Prairie Technologies (Middleton, WI), equipped with a 16X water-immersion objective lens (0.8 NA;CF175, Nikon). Two-photon excitation of the electrode and somata was used at 915nm (DeepSee femtosec laser, Spectraphysics) and the laser beam was extended to fill the large back aperture of the 16X objective.

Electrodes (5-10 MΩ) were pulled from filamented, thin-walled, borosilicate glass (outer

diameter, 1.5 mm; inner diameter, 1.0 mm; Hilgenberg GmbH, Malsfeld, Germany) on a vertical two-stage puller (PC-12, Narishige, EastMeadow, NY). Electrodes were filled with an internal solution containing (in mM): 140 K-gluconate, 10 KCl, 10 HEPES, 10 Na₂-Phosphocreatine, 4 MgATP, 0.4 Na₂GTP, 0.5 EGTA, pH adjusted to 7.25 with KOH. For electrode visualization the internal solution was supplemented with 200 μM Alexafluor 488 (Life technologies, Invitrogen). To minimize brain pulsations two percent low melting agar (type IIIa, Sigma-Aldrich, St. Louis, MO) was placed over the craniotomy. All recordings were acquired using an intracellular amplifier in current clamp mode (Multiclamp 700B, Molecular Devices), at a sampling rate of 10 kHz (Digidata 1440A, Molecular Devices, Sunnyvale, CA), and were filtered using a 50 Hz high pass filter. Recordings from PVNs^{EPL} and non-PVN^{EPL} were made strictly from the EPL (mean recording depth 186.76±42.13μm), and GC's were targeted by limiting the patch pipette depth to the GCL (i.e. >340μm; Figure 4A). Recording locations were widely distributed across the dorsal part of the OB, to minimize potential bias from sampling a spatially restricted population.

The electrode was directed toward the cells under visual guidance, to achieve loose patch configuration. Lateral excursions of the electrode were kept to distances less than 100 μm. Correct targeting was initially verified by visual guidance, and an increase in electrode resistance. Additionally, fluorescent dye from the electrode was electroporated into the cell using current pulses. Only tdTomato+ cells that were distinctly filled during this procedure were included in our dataset. For the control group of non-PVN^{EPL} cells, data was collected either by shadow patching (Kitamura et al., 2008) or by "blind" patching in the vicinity of tdTomato+ cells. Non-PVN^{EPL} cells were also filled after recording.

Respiration-Triggered Odor Delivery

Odor stimuli were delivered directly to the nose via a custom made 5-channel olfactometer with completely isolated odor channels to circumvent contamination between odors.

Upon odor delivery, the N₂ stream was switched into one of the odor vials for the desired duration, while the overall flow was kept constant. A custom-written MATLAB program controlling a Master-8 (A.M.P.I, Israel) was used to control the odor delivery from the olfactometer. A panel of 5 odors known to activate the dorsal part of the OB were used in all experiments (Luo and Katz, 2001; Reidl et al., 2007; Soucy et al., 2009). The odors (butanal, pentanal, ethyl tiglate, propanal and ethyl butyrate) were all obtained from Sigma-Aldrich. We limited the duration of our odor protocol to ~20 minutes, and to increase statistical power we used 4-10 trials/odor. The odors were presented for 2 secs, in pseudo-random order, with an inter-stimulus interval of 18 secs. Odors were first diluted in mineral oil according to their individual vapor pressures to give a nominal headspace concentration of 1000 ppm. Next, odors were further diluted with O₂ to achieve a final concentration of 50 ppm or 500 ppm. No significant differences between the average data of these concentrations were found so odor concentrations were pooled.

The animal's respiration was monitored throughout the experiment by a low pressure sensor

(1-INCH-D1-4V-MINI, by 'All sensors'). The low pressure sensor was connected to a thin stainless steel tubing (OD 0.7 mm) which was placed at the entrance of the animals' contra-lateral nostril. The information from the pressure sensor was passed to an analogue converter (window discriminator), which was used to identify the inhalation onset during the respiratory cycle. We then used a custom-written MATLAB program to trigger odor delivery at inhalation onset.

Electrophysiology Data Analysis

A custom-written MATLAB program was used to perform data analysis. Spikes were extracted from voltage traces using thresholding. Spike times were assigned to the local peaks of supra threshold segments and rounded to the nearest msec. Respiration cycle times were calculated by finding local minima and maxima in the respiration trace.

Throughout all trials, spontaneous firing rate was assessed by calculating the mean spontaneous firing rate based on the 4 secs period that preceded each stimulus. Spontaneous phase tuning was assessed by first assigning each spike its timing in the respiration cycle ($0-2\pi$), during the 2 secs preceding odor stimulation. Next, the cell's temporal spiking pattern was examined to determine whether it is significantly tuned to a certain phase in the respiration cycle, or is uniformly distributed throughout the cycle. In order to test for circular uniformity the Rayleigh test was used (Berens, 2009), significant phase tuning was accepted at $p < 0.01$. For significantly phase-tuned cells the mean angular direction of the spikes was calculated, as the phase in the respiration cycle to which the cell was tuned. Spike waveform of PVN^{EPL} was extracted and average spike waveform calculated using a custom-written MATLAB program. Using the average spike waveform two parameters were calculated: spike duration (between spike peak to volley) and the ratio between the amplitudes of the spike peak and volley (Cohen et al., 2011; McCormick et al., 1985; Niell and Stryker, 2008) (Figure S4).

Odor responses were defined as either changes in spike rate or changes in the angular distribution of spikes in the respiration cycle (changes in phase tuning), or both (e.g. Figure 5A- rate changes; 5B,C- phase tuning changes). Changes in spike rate were detected by comparing: (1) The mean firing rate in the 2 sec preceding odor onset to the mean firing rate during the entire 2 sec odor period, across all repetitions of the same odor. (2) The mean firing rate in the 2 sec preceding odor onset to the 2 sec after odor offset, across all repetitions of the same odor. (3) The average spike rate per respiration during the 2 secs preceding odor onset to the spike rate in each respiration during the odor period, across all repetitions of the same odor. For these comparisons a paired T-test was used, accepting significance at $p < 0.05$, except for the analysis of single respirations, in which case the Bonferroni correction for multiple comparisons we applied. Phase tuning responses were analyzed only if a cell showed significant phase tuning before and during the odor presentation. Phase tuning responses were detected by comparing the cell's phase tuning in the 2 secs preceding odor onset to the phase tuning during the 2 secs odor period, across all trials. For this comparison a multi-sample test for equal median directions was used (Berens, 2009).

Odor rate responses were classified as either excitatory (increase in spike rate) or inhibitory (decrease in spike rate). An odor response was considered inhibitory only if it was not preceded by an excitatory response, and *vice versa*. The percentage of excitatory versus inhibitory responses was calculated out of the total number of odor evoked changes in firing rate. Response magnitude was calculated as the absolute maximal change in firing rate either during the entire odor presentation or per respiration, across odors.

For the comparison of multiple groups, a one way ANOVA was used (significant accepted at $p < 0.01$) followed by post hoc pair-wise comparisons using Tukey's honestly significant difference criterion (Tukey's HSD, confidence interval 95%).

Significant differences between the percentages of cells/responses of different categories between groups were tested using a test for comparison of the proportions of two binomial variables (e.g. the percentage of excitatory versus inhibitory responses, Fig 5E).

Immunohistochemistry and Microscopy

For transsynaptic tracing experiments (Figure 1, 2, 6, and 7) brain tissue was processed according to previously described procedures (Espinosa et al., 2009; Miyamichi et al., 2011). To set the common coronal plane among different animals, the cerebellum was cut off, and the brain was embedded in the Optimum Cutting Temperature (O.C.T.) compound (Tissue-Tek) with the cutting surface facing the bottom of the mold. The brain was adjusted to ensure that the left-right axis was parallel to the section plane. Neither mCherry nor GFP required immunostaining for visualization. The following antibodies were used in the analysis of cell type of starter cells and trans-synaptically labeled neurons: rabbit anti-parvalbumin (1:2000, Swant), rabbit anti-tyrosine hydroxylase (1:500, Millipore, Cat#ab152), rabbit anti-calretinin (1:500, Abcam, Cat#ab702), rabbit anti-Tbr2 (1:500, Abcam, Cat#ab23345), and mouse anti-rabies glycoprotein (1:500, Millipore, Cat#mab8727). 60 μ m, free floating, coronal sections of the OB were treated for 1 hour at room temperature with 5% normal goat serum in phosphate buffer saline containing 0.3% Triton-X1000 (PBST). Tissues were then treated at 4 degrees free floating with primary antibodies in 0.3% PBST for 4 days. After washing three times for 10 min with 0.3% PBST, the sections were treated with goat anti-rabbit Alexa Fluor 647 or goat anti-mouse Alexa Fluor 488 (1:200, Jackson ImmunoResearch) at 4 degree for 2 days, followed by washing three times for 10 min with 0.3% PBST. Finally the sections were treated with PBS containing 4',6-diamidino-2-phenylindole dihydrochloride (DAPI; Sigma, Cat#D8417) or NeuroTrace Blue (1:500, Invitrogen, Cat#N-21479) for 20 min and mounted with cover glass using Fluorogel (Electron Microscopy Sciences, Cat#17985-10) Sections were imaged with a Nikon CCD camera by using a 10x objective or by 1.6-2.0 μ m optical sectioning using confocal microscopy (Zeiss 510 or 780).

For Figure 3A, coronal sections (40 μ m) of the OB were treated with anti-PV antibodies (Swant, rabbit anti-PV, 1:1000 in blocking solution) overnight, washed with PBS, and then incubated for another 2 hours with a secondary antibody (Chemicon, goat anti-rabbit-Cy5, 1:250). Slices were

imaged by Leica SP50 confocal microscope (Wetzlar, Germany), equipped with a 40X (1.25 NA) Leica oil objective (Wetzlar, Germany). Counting of neuronal somata was performed manually from the confocal images by choosing random regions of the EPL within the slices. Each somata was scored as labeled with tdTomato, Cy5, or both.

3D-Reconstruction and Quantitative Analysis.

The 3D-reconstruction and cylindrical coordinate systems for the OB and AON/APC were previously described (Miyamichi et al., 2011). To adjust the established programs for the current study, the following additions and modifications were made.

- 1) We generated a semi-automatic system to detect the MCL and EPL/GL boundary in each coronal section of the OB by processing the density distribution of the DAPI signal. For this, we utilized the fact that DAPI signal is significantly higher in the MCL and in the GL than in the EPL. To process an image of an OB section, we first removed background noise and performed Gaussian blurring of the DAPI signal. Next, DAPI signal intensity was measured along each radiation axis of the OB (a ray starting from the center of the OB and extending outwards) at 1 degree intervals. The DAPI intensity moving along each radiation angle would be high in the GCL/MCL, drop in the EPL, and rise again in the GL. Therefore, when DAPI intensity is plotted along each radiation angle, the first falling edge corresponds to the MCL and the subsequent rising edge corresponds to the EPL/GL boundary. The MATLAB processing detected these boundary points, and in addition, tracked the boundary points that were detected at neighboring radiation angles to check that the detected boundaries remained continuous. The MCL and EPL/GL boundary were thereby marked by a dense series of points, which were then recorded into Scalable Vector Graphics (SVG) format. The entire process was implemented in a MATLAB program that ran automatically with human correction when necessary.
- 2) After plotting the MCL and EPL/GL boundary, we manually annotated starter cells and GFP-labeled presynaptic neurons using dots of different colors to represent cells of different layers and types. This manual annotation was carried out in Adobe Illustrator and stored in an SVG file, which was read by MATLAB. We used the mass center for all dots that corresponded to the MCL and EPL/GL layers to approximate a single point representing the mass center of a slice. The precise slice centering and rotation, assembly of multiple slices, and setting the polar axis were performed as previously described (Miyamichi et al., 2011). The only modification is that instead of aligning complete glomeruli between slices, the EPL/GL boundary was used for alignment. These two methods give similar results. All steps after manual annotation of GFP labeled cells were automatically done by MATLAB without human intervention to avoid biasing the registration results. These MATLAB scripts are available upon request.
- 3) For AON/APC reconstruction (figure S6), we increased the number of colors during the manual annotation of labeled cells such that neurons in the different anatomical structures (e.g., AON or APC) can be mapped by distinct colors.

We used Paraview (version 3.98) to visualize the Visualization Toolkit (VTK) format file of 3D reconstructed OB and AON/APC.

For the distribution of θ and Z analysis, we pooled θ and Z values from multiple experiments as individual samples contained relatively small number of starter cells for the statistical analysis. Because location of starter cells was slightly different between the each sample, we normalized the data by a uniform transformation to each OB such that the median θ_{starter} and median Z_{starter} turn to an identical value among multiple samples. In *Pcdh21-Cre* experiments (Figure 2D, 7D), median $\theta_{\text{starter}} = 0.96 \pm 0.03 \pi$ and median $Z_{\text{starter}} = 0.63 \pm 0.047$ (n=3 animals) were normalized to $\theta'_{\text{starter}} = 1.00\pi$ and $Z'_{\text{starter}} = 0.600$, respectively. In the *PV-Cre* experiments (Figure 6D), median $\theta_{\text{starter}} = 0.92 \pm 0.025 \pi$ and median $Z_{\text{starter}} = 0.46 \pm 0.035$ (n=7 samples) were normalized to $\theta'_{\text{starter}} = 1.00\pi$ and $Z'_{\text{starter}} = 0.490$, respectively. In the histogram (Figure 2D, 6D, 7D, S2C, and S3D), individual bin size was $1/45 \pi$ for θ' , and 0.02 for Z' , except for Fig 7D top panels, where the bin sizes was $1/18 \pi$ for θ and 0.02 for Z .

Supplemental References

- Berens, P. (2009). CircStat: A MATLAB Toolbox for Circular Statistics. *J Stat Software* 31.
- Brunjes, P.C., Illig, K.R., and Meyer, E.A. (2005). A field guide to the anterior olfactory nucleus (cortex). *Brain Res Brain Res Rev* 50, 305-335.
- Cohen, L., Rothschild, G., and Mizrahi, A. (2011). Multisensory integration of natural odors and sounds in the auditory cortex. *Neuron* 72, 357-369.
- Espinosa, J.S., Wheeler, D.G., Tsien, R.W., and Luo, L. (2009). Uncoupling dendrite growth and patterning: single-cell knockout analysis of NMDA receptor 2B. *Neuron* 62, 205-217.
- Hippenmeyer, S., Vrieseling, E., Sigrist, M., Portmann, T., Laengle, C., Ladle, D.R., and Arber, S. (2005). A developmental switch in the response of DRG neurons to ETS transcription factor signaling. *PLoS Biology* 3, e159.
- Huang, L., Garcia, I., Jen, H.I., and Arenkiel, B.R. (2013). Reciprocal connectivity between mitral cells and external plexiform layer interneurons in the mouse olfactory bulb. *Frontiers Neural Circuits* 7, 32.
- Kitamura, K., Judkewitz, B., Kano, M., Denk, W., and Häusser, M. (2008). Targeted patch-clamp recordings and single-cell electroporation of unlabeled neurons in vivo. *Nat Methods* 5, 61-67.
- Lepousez, G., Csaba, Z., Bernard, V., Loudes, C., Videau, C., Lacombe, J., Epelbaum, J., and Viollet, C. (2010). Somatostatin interneurons delineate the inner part of the external plexiform layer in the mouse main olfactory bulb. *J Comp Neurology* 518, 1976-1994.
- Luo, M., and Katz, L.C. (2001). Response correlation maps of neurons in the mammalian olfactory bulb. *Neuron* 32, 1165-1179.

- McCormick, D.A., Connors, B.W., Lighthall, J.W., and Prince, D.A. (1985). Comparative electrophysiology of pyramidal and sparsely spiny stellate neurons of the neocortex. *J Neurophysi* *54*, 782-806.
- Miyamichi, K., Amat, F., Moussavi, F., Wang, C., Wickersham, I., Wall, N.R., Taniguchi, H., Tasic, B., Huang, Z.J., He, Z., *et al.* (2011). Cortical representations of olfactory input by trans-synaptic tracing. *Nature* *472*, 191-196.
- Niell, C.M., and Stryker, M.P. (2008). Highly selective receptive fields in mouse visual cortex. *J Neurosci* *28*, 7520-7536.
- Reidl, J., Starke, J., Omer, D.B., Grinvald, A., and Spors, H. (2007). Independent component analysis of high-resolution imaging data identifies distinct functional domains. *NeuroImage* *34*, 94-108.
- Rong, L., Gendron, K., Strohl, B., Shenoy, R., Wool-Lewis, R.J., and Bates, P. (1998). Characterization of determinants for envelope binding and infection in tva, the subgroup A avian sarcoma and leukosis virus receptor. *J Virology* *72*, 4552-4559.
- Seidler, B., Schmidt, A., Mayr, U., Nakhai, H., Schmid, R.M., Schneider, G., and Saur, D. (2008). A Cre-loxP-based mouse model for conditional somatic gene expression and knockdown in vivo by using avian retroviral vectors. *Proc Natl Acad Sci U S A* *105*, 10137-10142.
- Soucy, E.R., Albeanu, D.F., Fantana, A.L., Murthy, V.N., and Meister, M. (2009). Precision and diversity in an odor map on the olfactory bulb. *Nat Neurosci.* *12*, 210-220.
- Tasic, B., Miyamichi, K., Hippenmeyer, S., Dani, V.S., Zeng, H., Joo, W., Zong, H., Chen-Tsai, Y., and Luo, L. (2012). Extensions of MADM (mosaic analysis with double markers) in mice. *PloS One* *7*, e33332.
- Wall, N.R., Wickersham, I.R., Cetin, A., De La Parra, M., and Callaway, E.M. (2010). Monosynaptic circuit tracing in vivo through Cre-dependent targeting and complementation of modified rabies virus. *Proc Natl Acad Sci U S A* *107*, 21848-21853.
- Watabe-Uchida, M., Zhu, L., Ogawa, S.K., Vamanrao, A., and Uchida, N. (2012). Whole-brain mapping of direct inputs to midbrain dopamine neurons. *Neuron* *74*, 858-873.
- Wickersham, I.R., Lyon, D.C., Barnard, R.J., Mori, T., Finke, S., Conzelmann, K.K., Young, J.A., and Callaway, E.M. (2007). Monosynaptic restriction of transsynaptic tracing from single, genetically targeted neurons. *Neuron* *53*, 639-647.
- Wickersham, I.R., Sullivan, H.A., and Seung, H.S. (2010). Production of glycoprotein-deleted rabies viruses for monosynaptic tracing and high-level gene expression in neurons. *Nat Protoc* *5*, 595-606.